Supplementary Information:

Strong constraints on aerosol-cloud interactions

from volcanic eruptions

Malavelle et al.

Methods

M1. Description of the IASI algorithm and retrievals

Only recently has it been recognised that in favourable conditions (large column burdens coupled with large thermal contrasts and/or a dry atmosphere) hyper-spectral infrared sounders are sensitive to lower tropospheric SO_2[50]. Despite this, satellite retrievals of lower tropospheric SO_2 from the 2014-15 Holuhraun eruption remain very challenging for both ultraviolet/visible (UV/VIS) and infra-red (IR) instruments. In what follows, an overview is given of the IASI algorithm used here and its associated uncertainties. The measurements are also briefly compared with independent satellite retrievals[32,51] of IASI and OMI (Ozone Monitoring Instrument).

The IASI SO_2 retrieval algorithm consists of two independent steps, Firstly, an estimate of the SO_2 altitude is made using the algorithm developed to study plume heights of the 2011 Nabro eruption[52]. Here we use an updated (global) version of the algorithm[50] and perform all calculations in the $1,300-1,410$ cm^{-1} spectral range. Secondly, the method used to retrieve the SO_2 column[50,51] is an optimal estimation retrieval using a generalised noise covariance matrix ($S\varepsilon$). The $S\varepsilon$ and the associated mean residual have been calculated in the $1,300-1,410$ cm^{-1} spectral range[51], using 15,000 couples of IASI spectra and forward simulations randomly chosen in time and space. The a priori profile of SO_2 was taken to be zero at all altitudes except the retrieved altitude where it was set to 100 times the US standard atmosphere[53] volume mixing ratio.

Retrievals have been performed on all IASI data recorded in the area 60°W-30°E/45°N-80°N. One of the main sources of uncertainty on the retrieved SO_2 columns comes from errors on the retrieved altitude. The uncertainty in the retrieved SO_2 altitudes from IASI is of order of 1 km high up in the troposphere[51], but larger errors could be expected closer to the surface. Test cases have been performed assuming a generous error bar of ±2 km for altitudes below 4 km. These typically translate into errors of the order a factor 2 on the column (an underestimate on the altitude leads to an overestimate on the column and vice versa). Other sources of errors include the presence of clouds (which generally leads to underestimations if the SO_2 lies above cloud or missing data if the SO_2 lies below cloud) and the presence of IASI pixels containing SO_2 columns below IASI's detection limit (pixels for which the detection algorithm indicated no SO_2 were set to 0 DU).

Overall, we estimate the uncertainty on the individual SO_2 columns to be at least 50%. SO_2 total mass burdens have been calculated for morning and evening overpasses. We found that, especially for narrow plumes, the gridding procedure and grid box sizes also had a non-negligible effect on the calculation of these burdens.

Considering only morning measurements, we find an average daily mass burden of 5,630 kt of SO_2 for September 2014 and of 3,121 kt for October 2014. Taking also into account the evening measurements, the averages slightly decrease to 5,230 kt for September and 3020 kt for October. These are in excellent agreement with the independent IASI retrievals reporting (for an area of 60°W-40°E/45°N-75°N) for September a value of 61±18 kt considering only morning overpass and of 55±17 kt considering all the measurements[32]. Masses estimated from OMI are considerable larger, totalling on average 99±49 kt for September[32,50].

M2. Description of HadGEM3 and simulations

HadGEM3 is an updated version of the well documented HadGEM2 model[54]. Major advances relative to HadGEM2 include a revised treatment of warm rain processes[55] and the UKCA/ GLOMAP-mode chemistry/aerosol scheme[39] which is a two-moment aerosol microphysics scheme allowing better representation of aerosol processes such as nucleation, coagulation, condensation and internal mixing. Simulations were performed with the atmosphere-only component of HadGEM3, a developmental version of the GA7.0 global atmosphere model, the successor to the atmospheric component of the GC2.0 global coupled configuration of the Met Office's Unified Model[56]. The N96 resolution model used here has a resolution of 1.25° in latitude by 1.875° in longitude and has 85 atmospheric layers up to an altitude of about 85 km.

The version used here differs slightly from the finalised GA7.0 in the following ways: different tunings for the convective detrainment, non-orographic gravity-wave drag and mineral dust aerosol schemes; the width of the probability distribution function of cloud-scale updraught in the aerosol activation scheme is capped at 0.4 m.s^{-1}; interactive (rather than prescribed) oxidants are used in the UKCA/GLOMAP-mode atmospheric chemistry/aerosol scheme; and an improved tracer advection scheme is used[57].

The spatial and temporal emissions of SO_2 from industrial and natural sources are represented[58]. To capture the prevailing meteorological conditions, the horizontal wind fields and the potential temperature in the simulations were nudged[59] to ERA-Interim reanalyses[60] and used updated HadISST data[61] to provide observationally-based monthly sea-surface temperature and sea-ice boundary conditions. All simulations for each year are 3 months long starting on the 1st August and continue through until the end of October. Simulations that include the 2014-15 Holuhraun eruption assume that the eruption commences on 31st August 2014.

M3. Description of data processing of IASI and HadGEM3 SO₂ data

The evolution of the plume for HadGEM3 and for IASI at their native resolutions using data from HadGEM3 from the nearest timestep to the IASI morning (AM) and afternoon (PM) overpasses are available as an animation (SI-SO2-Animation.mp4). The model is able to represent the general features observed in the IASI plume indicating that the nudging scheme is effective in representing the meteorological evolution of the plume.

In order to make a more quantitative assessment of the performance of HadGEM3, IASI products are first remapped to N96 resolution using the Climate Data Operators libraries (https://code.zmaw.de/projects/cdo) for both AM and PM overpasses. The scarcity of positive IASI detection introduces a large amount of missing data owing to a combination of cloud impacts and SO₂ detection limits. Interpolation procedures and remapping of the hi-resolution data proves challenging on some occasions. Comparing the different remapping techniques, we found that a bilinear interpolation procedure introduced the smallest errors (about 15%) in the resulting SO₂ domain averages.

Once IASI data have been regridded, we perform basic plume detection on both datasets by screening pixels for which the SO₂ column burden is found to be less than 0.05 Dobson Units and create two plume masks, M1 and M2, for IASI and HadGEM3 respectively. Although this threshold could be considered as rather low and allows for European SO₂ emissions to be included in the HadGEM3 data, the IASI algorithm does not detect low level background SO₂ from European emissions. These pixels are subsequently removed as we will explain below. We seek to compare the domain averaged SO₂ concentration from the model and from the observations. Because of the limited number of positive detections in the IASI dataset, it is hard to establish a robust procedure and evaluate potential impact of spatial displacement errors[62]. Therefore, we opt for a simple point-to-point comparison by sampling pixels collocated in space and time in both datasets (i.e. retaining pixels corresponding to the intersection of M1 and M2). These pixels are used to compute the instantaneous domain averages for the AM and PM overpasses for each day.

M4. Description and processing of the MODIS data

In order to quantify the impact of the volcanic emissions on clouds properties, we used the level 3.0 datasets at collection version 051 derived from the MODIS observations on the AQUA platform (MYD08 products 1 by 1 degree aggregation of the MYD06 pixel-level products, http://modis-atmos.gsfc.nasa.gov/_docs/C6MOD06OPUserGuide.pdf). Technically, MODIS measures radiances at different wavelengths and therefore does not measure any properties directly; measured radiances and radiative transfer modelling are used to retrieve cloud effective radius (r_{eff}) and cloud optical depth (τ_{cloud}) from which other properties such as cloud liquid water path (LWP) are derived (https://modis-atmos.gsfc.nasa.gov/_docs/atbd_mod05.pdf). A description of the procedure for obtaining gird-box mean data from MODIS is provided here http://modis.gsfc.nasa.gov/data/

dataprod/pdf/MOD_08.pdf. Retrievals from the MODIS instrument on TERRA were also analysed but we didn't report the results as noticeable biases appear due to degradation of the instrument over the years[34] (Supplementary S3). Retrievals from the recently distributed Collection 006 mostly correct the issue and the results using this collection[29] are consistent with our analysis using collection 051. We used quality assured data (QA flagged variable) from the MYD08 dataset. While MODIS reports r_{eff} and LWP as standard retrievals in the MOD08 data set, cloud droplet number concentration (N_d) is derived from relationships[63] linking it to r_{eff} and LWP assuming that clouds are adiabatic, that N_d is invariant throughout the cloud, and assuming relationships between r_{eff} and the volumetric mean radius of the clouds[64].

To make the most like-with-like comparison of MODIS data with model data, we convert the in-cloud liquid water path (LWP_{in_cloud}) that is derived as a standard 1°x1° daily mean MYD08 product to a grid-box mean LWP by multiplying the daily mean MYD08 in-cloud LWP by the MYD08 liquid cloud fraction and aggregating this product ($LWP_{gridbox}$) up to a monthly mean. This means that we are comparing grid-cell averages from MODIS to grid-cell averages from the model. For intensive liquid cloud properties, such as liquid effective radius r_{eff}, the monthly means are calculated using the daily mean MYD08 r_{eff} weighted by liquid fraction pixel count and aggregated up to a monthly mean (similar to the procedure used in the standard MYD08_M3 product). The multi-year time-series of monthly means is used to calculate specific month climatology using data from the years 2002 to 2013, e.g. for September cloud effective radius climatology: $r_{eff\_SEP\_clim} =$ average$\{r_{eff\_SEP\_i}\}$ where i is the corresponding index for year 2002 to 2013. Anomalies (e.g. r_{eff}) are calculated by subtracting the aforementioned climatology from the respective monthly mean of a given year, e.g. for September 2014 cloud effective radius anomalies: $r_{eff\_SEP\_2014} = r_{eff\_SEP\_2014} - r_{eff\_SEP\_clim}$.

Supplementary Discussion

S1. Assessment of the performance of the model in capturing the magnitude and variability of the SO$_2$ plume

2D maps for each day resulting from the sub-sampling procedure are temporally averaged over windows of 7 days including both AM and PM samples (as shown in the main text, Figure 1). Only regions where the number of collocated pixels is greater than 2 during a given week are considered. The resulting daily and weekly composites are averaged to construct the daily and weekly time series displayed in Figure S1.1. The envelopes in Figure S1.1d represent the estimated error bars. For IASI, this uncertainty in SO$_2$ concentration is around 50% (Supplementary Information, Methods M1). To evaluate the uncertainty for HadGEM3, we assume that uncertainty in SO$_2$ concentration is, to first order, driven by uncertainty in emissions. Emissions during the first two weeks of the eruption were in the range of 80-120 kt[SO$_2$]/day. We estimate a 40% uncertainty in HadGEM3 SO$_2$ concentrations derived from the product of a factor of 1.2 uncertainty in emission and a factor of 1.15 uncertainty in interpolation procedures.

The temporal emissions in SO$_2$ for the STAN (detailed in Table S1.1) and 40KT case are shown in Figure S1.1a. The considerable variability in the plume column loading is driven by daily variability in the meteorology and the limited domain of the study as some SO$_2$ is periodically advected out of the domain of investigation. Generally, the variability is well represented in the model with the sharp peaks in column loading during days 5-7 and day 11 and the broad peaks between days 40-50 and days 50-60 being captured. Figures S1.1b and S1.1c show that the estimates using the temporally evolving emissions (STAN) are in much better agreement with the observations than those from 40KT, particularly during the first three weeks of the eruption. Throughout October 2014 there is quantitatively good agreement between the STAN simulation and the IASI observations.

STAN Emission rates				
Days since 31st of August	0-13	14-30	31-37	38-91
SO$_2$ emissions [kT SO$_2$/day]	100	57.5	80	45

Table S1.1. The surface emissions of sulphur dioxide from STAN experiment. Emissions are located in the model gridbox containing Holuhraun location (64.9°N;16.8°W).
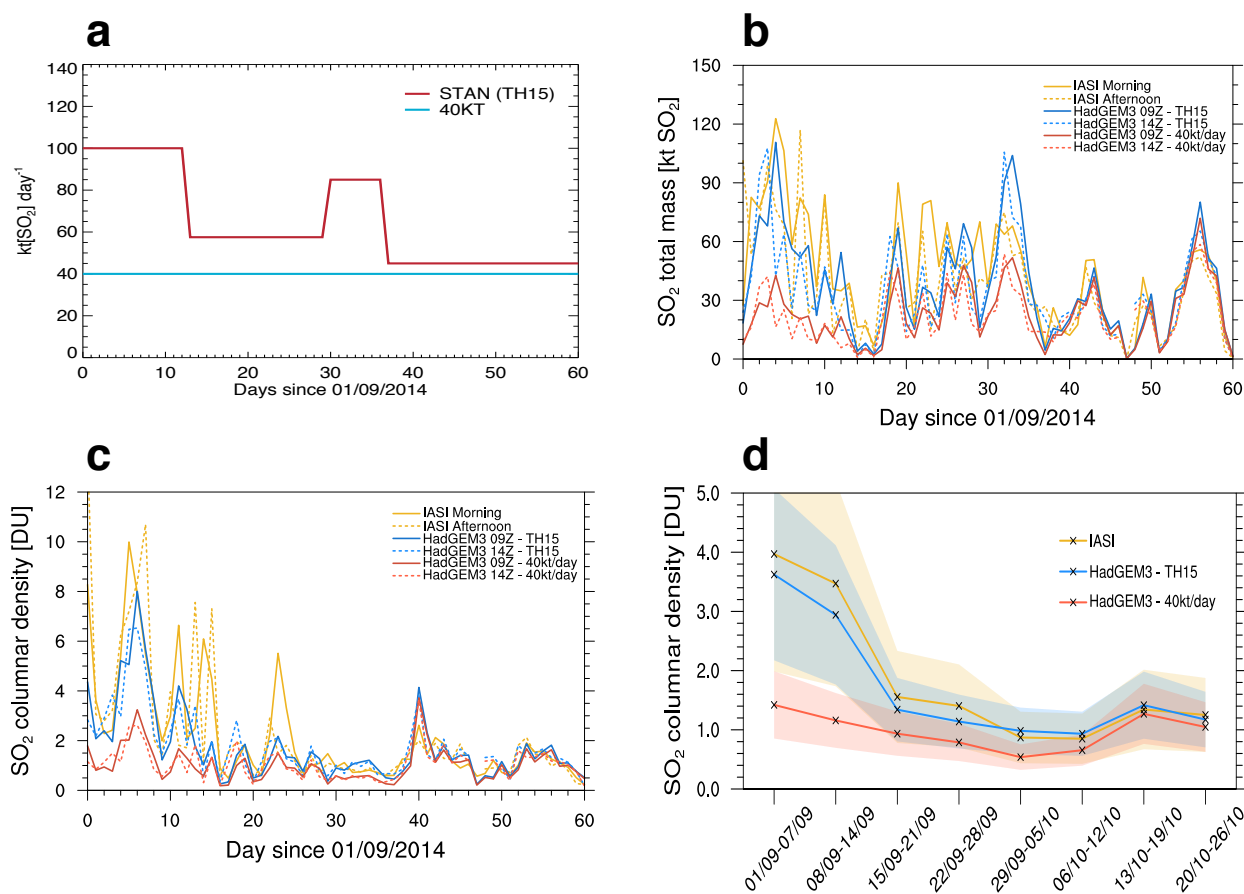
Figure S1.1. The temporal evolution of sulphur dioxide. *a) The temporal evolution of the emissions in kT[SO₂] per day. b) The temporal evolution of the in-plume SO₂ total mass in kT[SO₂] using the daily-mean data from the IASI sensor and that derived from the HadGEM3 STAN (denoted TH15 in the Figures) and 40KT simulation. c) The temporal evolution of the in-plume SO₂ column loading in Dobson Unit (DU) derived from daily-mean data and d) derived from weekly-mean data. The shaded envelope in d) represents an estimate of the uncertainty in the model and the observations.*

S2. Analysis of the perturbation to aerosol optical depth

The modelled Aerosol Optical Depth (AOD) anomalies for September and October 2014 caused by the 2014-15 eruption at Holuhraun (HOL_{2014}-NO_HOL_{2014}) shown in Figure S2.1 are influenced by the meteorological conditions that prevail during the month. There is a strong spatial coherence between the perturbation to the AODs and Δr_{eff} shown in Figure 3 in the main manuscript and Figure S5.1 in the supplementary.

SI-Cloud-Animation.mp4 demonstrates that it is virtually impossible to detect the perturbation to the AOD in the MODIS 1x1 degree monthly mean data predominantly because of the ubiquitous presence of cloud which makes AOD retrievals very scarce and the intersection of the volcanic plume and cloud free conditions scarcer still.
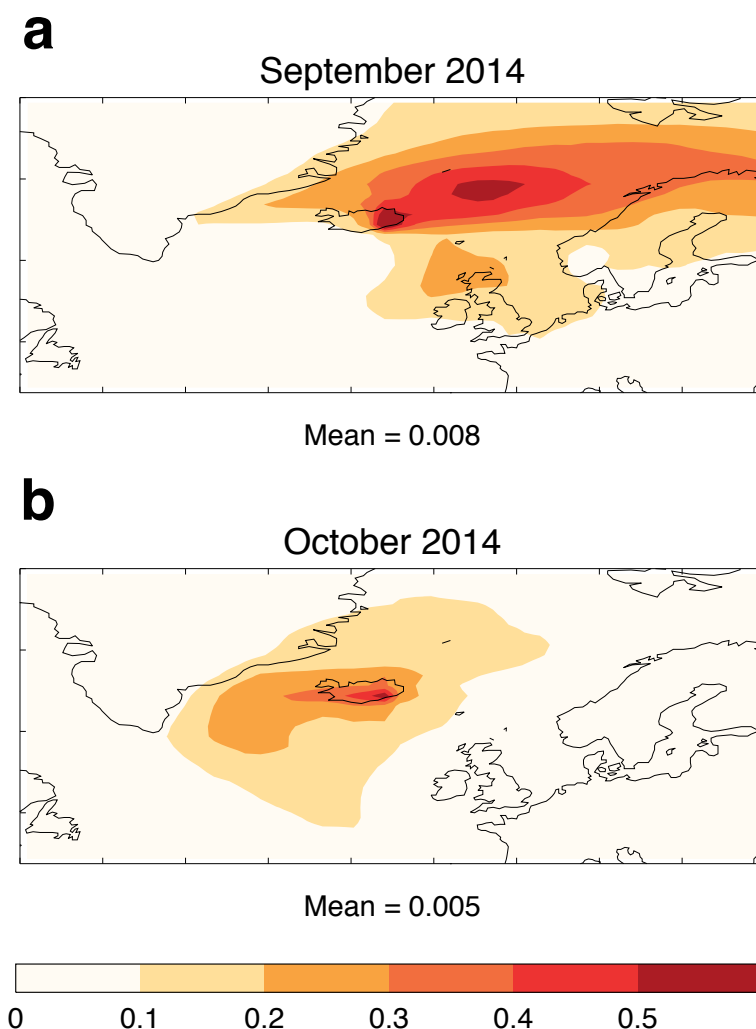
a

September 2014

Mean = 0.008

b

October 2014

Mean = 0.005

0   0.1   0.2   0.3   0.4   0.5

Figure S2.1. The modelled AOD perturbation from HadEGEM3 using UKCA. *Perturbations for a) September and b) October 2014. The AOD are calculated at the 550 nm wavelength.*

S3. Choice of MODIS platform

We investigate whether there are any systematic trends in r_{eff}, LWP and τ_{cloud} in products from both the TERRA and AQUA satellites. The motivation is that Collection 051 quality assured data from TERRA is subject to a degradation in the short wavelength channels, which has been shown to influence retrievals of surface reflectance[34]. Figure S3.1 shows that over the region of investigation for the TERRA instrument there are clear trends in LWP and τ_{cloud} while there is a smaller trend for r_{eff}. This may be explained by considering that MODIS retrievals of LWP and τ_{cloud} are most sensitive to shorter wavelengths (i.e. 0.86 µm) while r_{eff} is sensitive to longer wavelengths (i.e. 1.63 µm); the degradation of sensors has been shown to be greater at short wavelengths leading to more significant impacts on LWP and τ_{cloud}. Any such trends in AQUA data are much smaller and hence the analysis we present uses MODIS AQUA Collection 051 Quality Assured data.
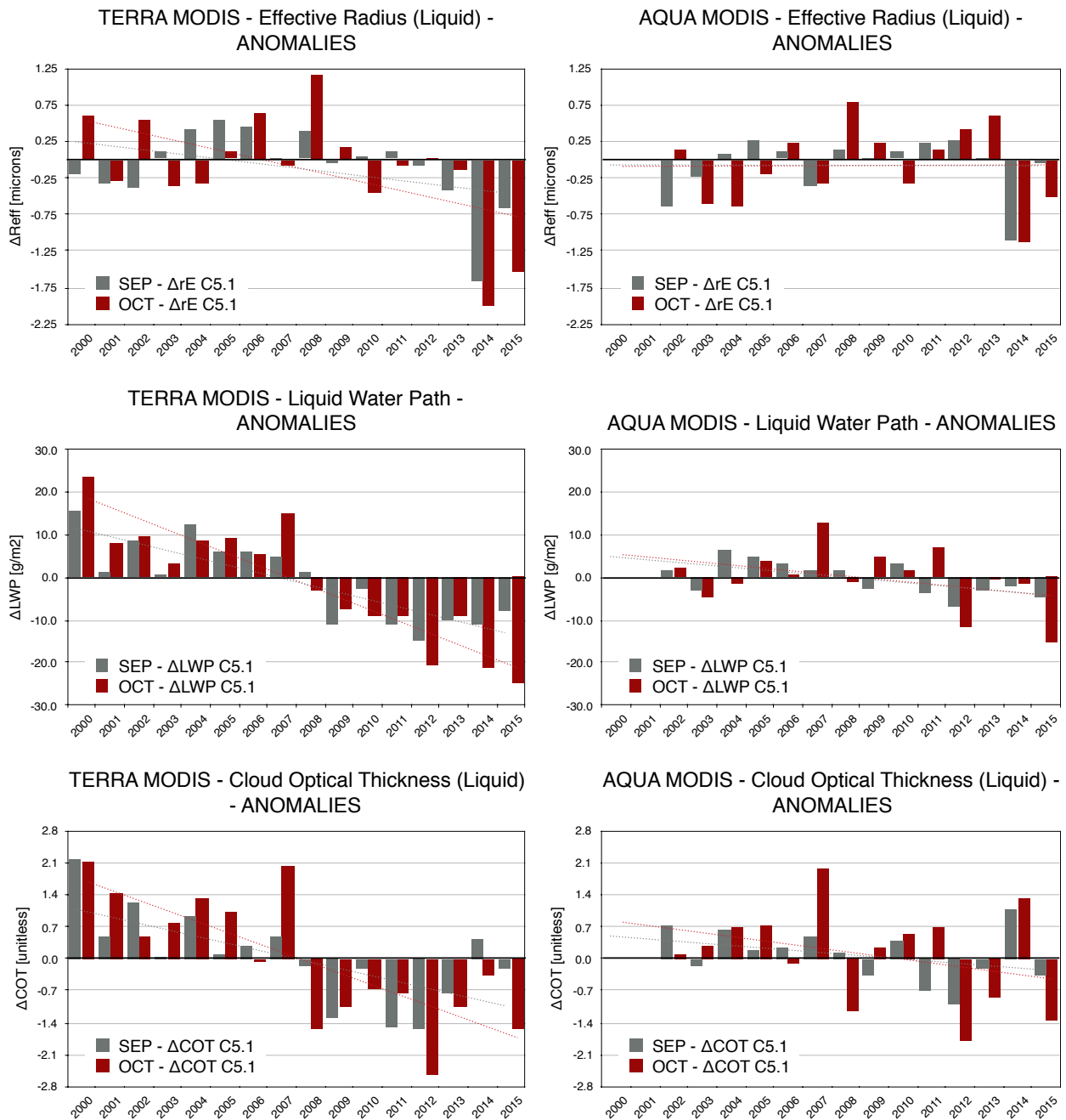
Figure S3.1. The evolution of the September and October cloud property anomalies from MODIS on AQUA and MODIS on TERRA spacecrafts*. Anomalies in r_{eff} (first row), LWP (middle row) and τ_{cloud} (last row) calculated with respect to their respective long-term means over the years 2000 to 2015 (data record starts in 2002 for AQUA). Data from TERRA are shown in the first column and data from AQUA in the second column. Lines represent linear fits to the data.*

S4. Year by year analysis of Δr_{eff}

While the MODIS retrievals show some reduced values for r_{eff} in various years (e.g. September 2002 and October 2007), the largest perturbations are obviously during September and October 2014 (Figure S4.1 and S4.2). Similar plots derived from HadGEM3 are shown in Figures S4.3 and S4.4. For HadGEM3 simulations, we can make similar conclusions to those from MODIS; the simulations including the 2014-15 eruption at Holuhraun yield the largest perturbations in r_{eff} in September 2014 and October 2014. The pattern in modelled Δr_{eff} is also similar to that in MODIS data in September 2002 which suggests that the model is capable of representing natural variability such as the enhanced aerosol concentrations advected off the coast of Europe in easterly flow regimes. The model also suggests a smaller Δr_{eff} close to Europe in Sept 2014 in the absence of the volcanic emissions; a more detailed analysis is warranted and is presented in supplementary section S6.
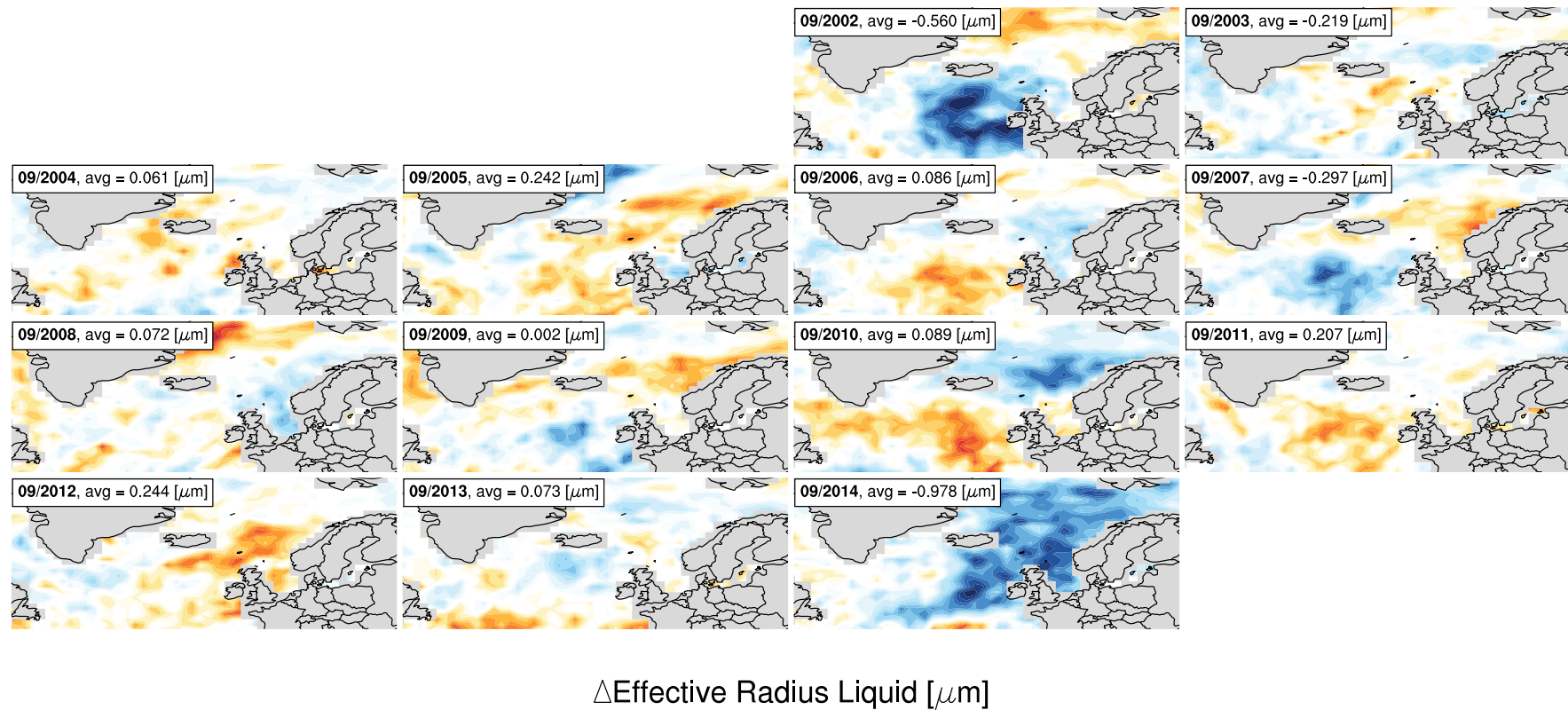
Figure S4.1. The effective radius anomalies during September months from MODIS. *Showing Δr_{eff} for each individual September month derived as the difference in annual monthly mean from the multi-year (2002-2013) September mean. In each case 'avg' represents the average anomalies.*
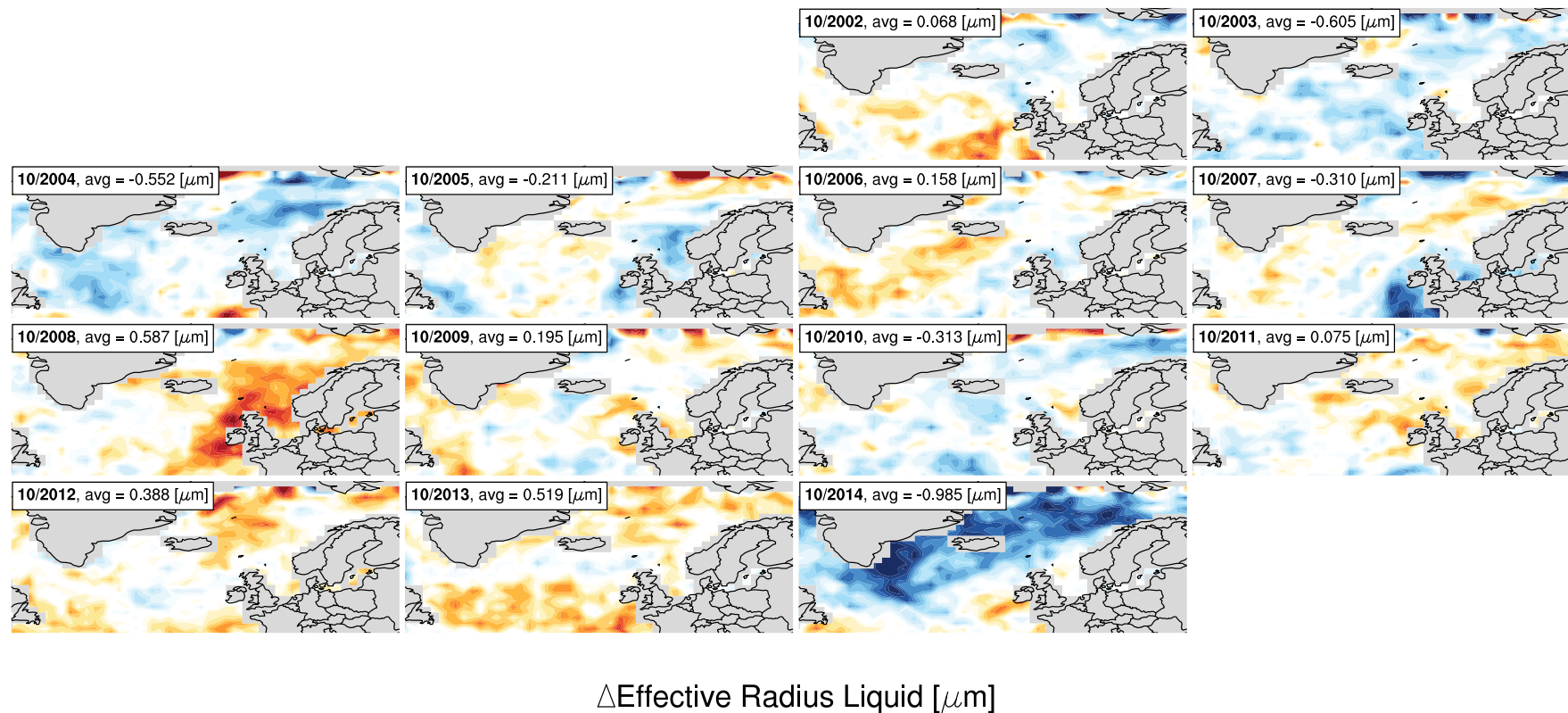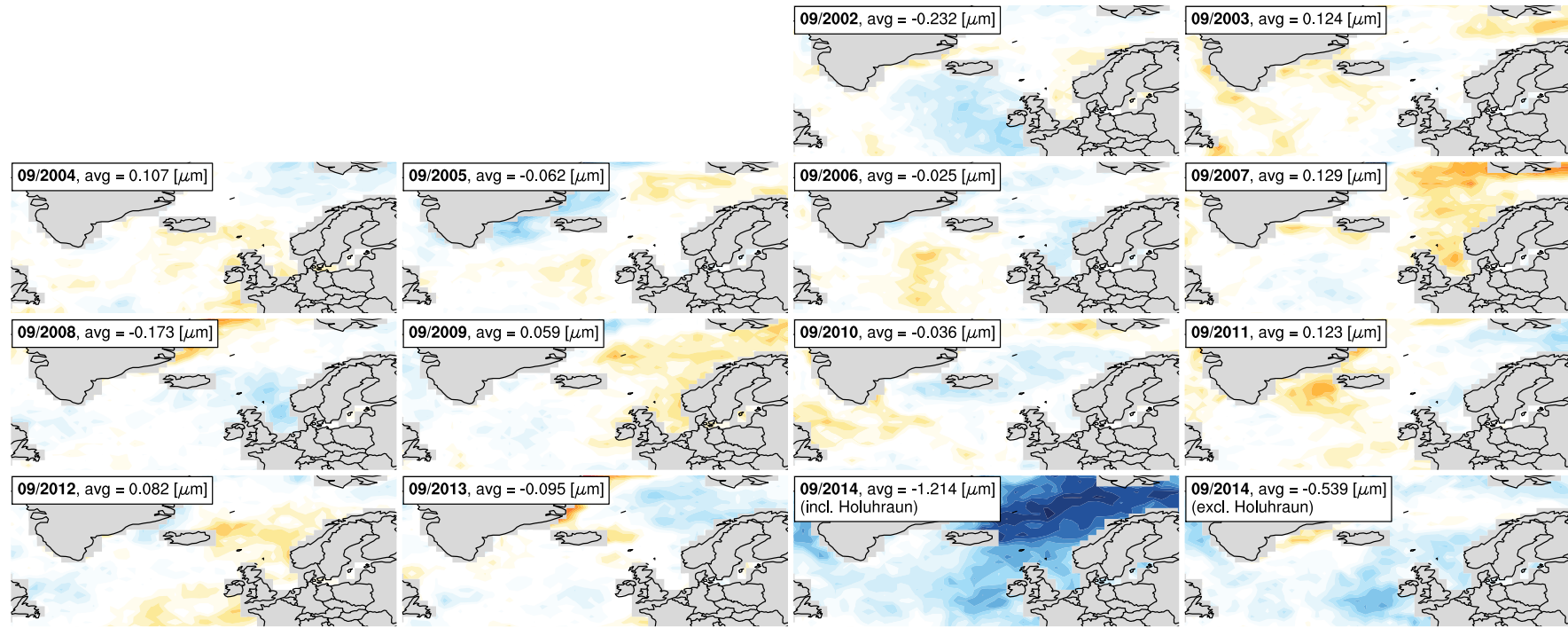
Figure S4.2. The effective radius anomalies during October months from MODIS. *Showing Δr_{eff} for each individual October month derived as the difference in annual monthly mean from the multi-year (2002-2013) October mean. In each case 'avg' represents the average anomalies.*
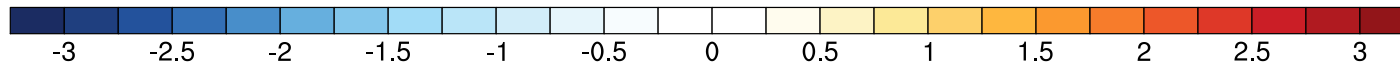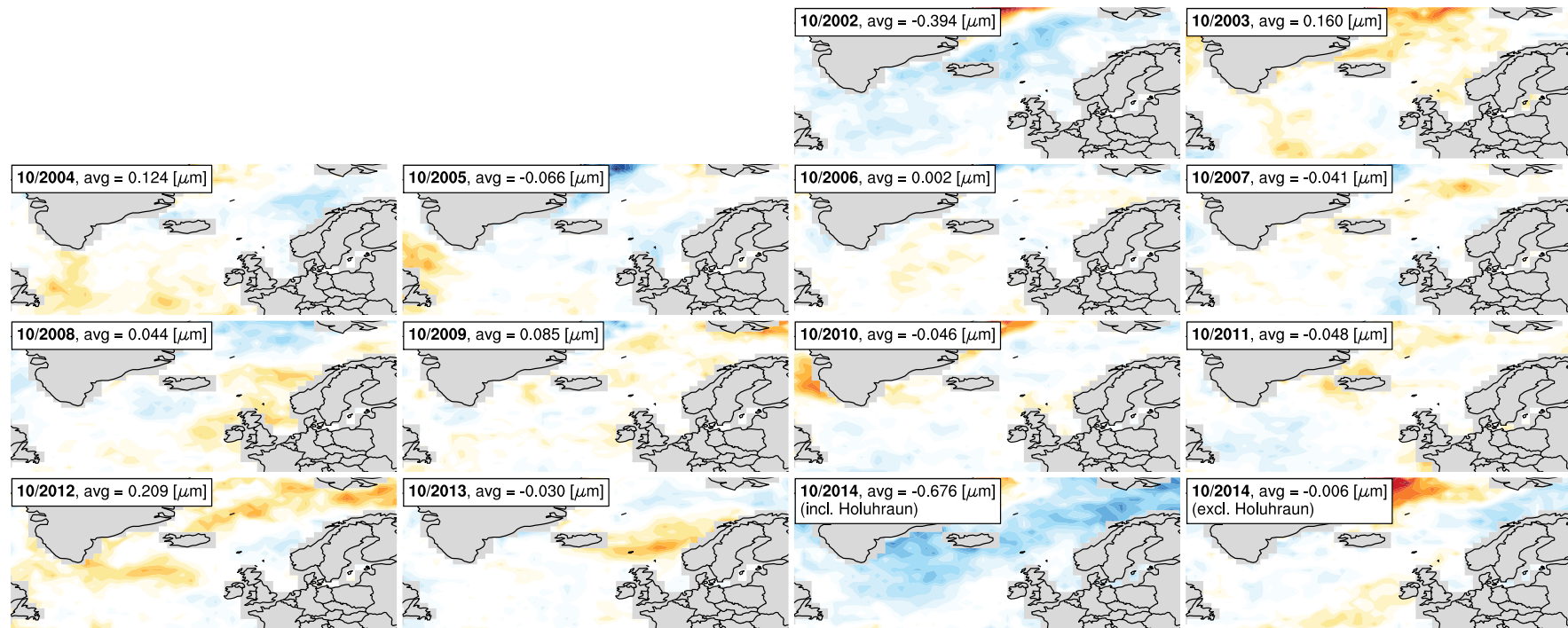
Figure S4.3. The effective radius anomalies during September months from HadGEM3 using UKCA. *Showing Δr_{eff} for each individual September month derived as the difference in annual monthly mean from the multi-year (2002-2013) September mean. The lower right hand panel shows simulations when the 2014-15 eruption at Holuhraun is excluded. In each case 'avg' represents the average anomalies.*
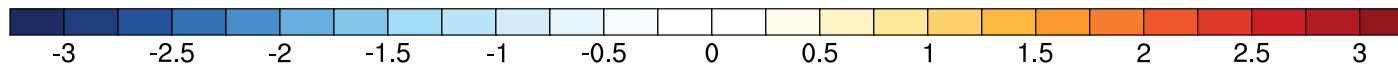
Figure S4.4. The effective radius anomalies during October months from HadGEM3 using UKCA. *Showing Δr_eff for each individual October month derived as the difference in annual monthly mean from the multi-year (2002-2013) October mean. The lower right hand panel shows simulations when the 2014-15 eruption at Holuhraun is excluded. In each case 'avg' represents the average anomalies.*

S5. Changes in cloud properties for September 2014

Figure 2 and Figure 3 (Main text) show the changes in cloud r_{eff} and LWP during October 2014 from MODIS and HadGEM3 respectively. These figures are reproduced for September 2014 in this section (Figure S5.1 and S5.2).
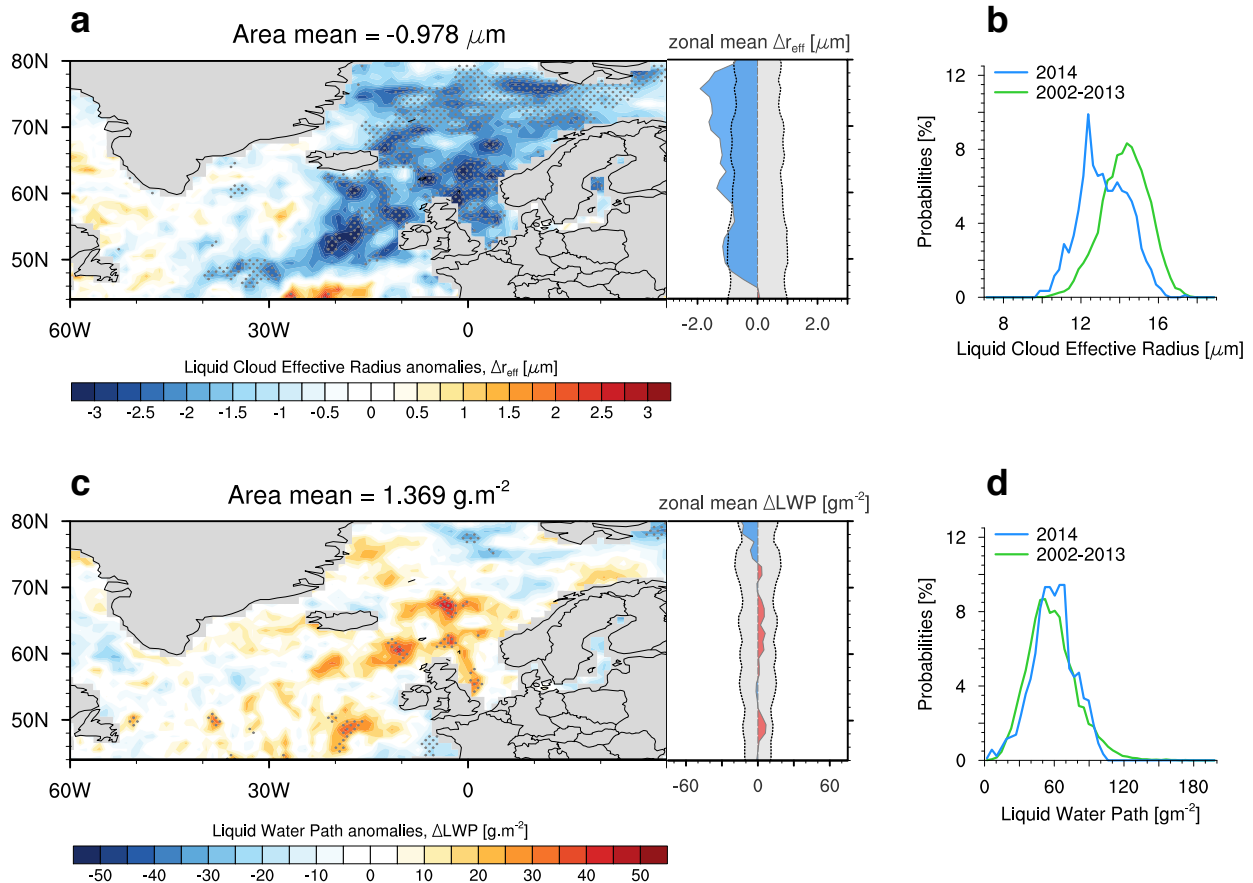

AQUA MODIS - September 2014

Figure S5.1. Changes in cloud properties as detected by the MODIS instrument on AQUA for September 2014. *The changes in (a) cloud droplet effective radius (μm) and (c) liquid water path (g.m^{-2}) with corresponding zonal means attached. The probability distributions of absolute cloud droplet effective radius (b) and liquid water path (d) for the year 2014 (blue) and the 2002-2013 long-term mean (green). Changes correspond to the deviation from the 2002-2013 long-term mean. Stippling in a) and c) represent areas where there is a significant perturbation at 95% confidence level based on a two-tailed Student's t-test. Grey shading in the zonal means represent the standard deviation over the 2002-2013 period.*
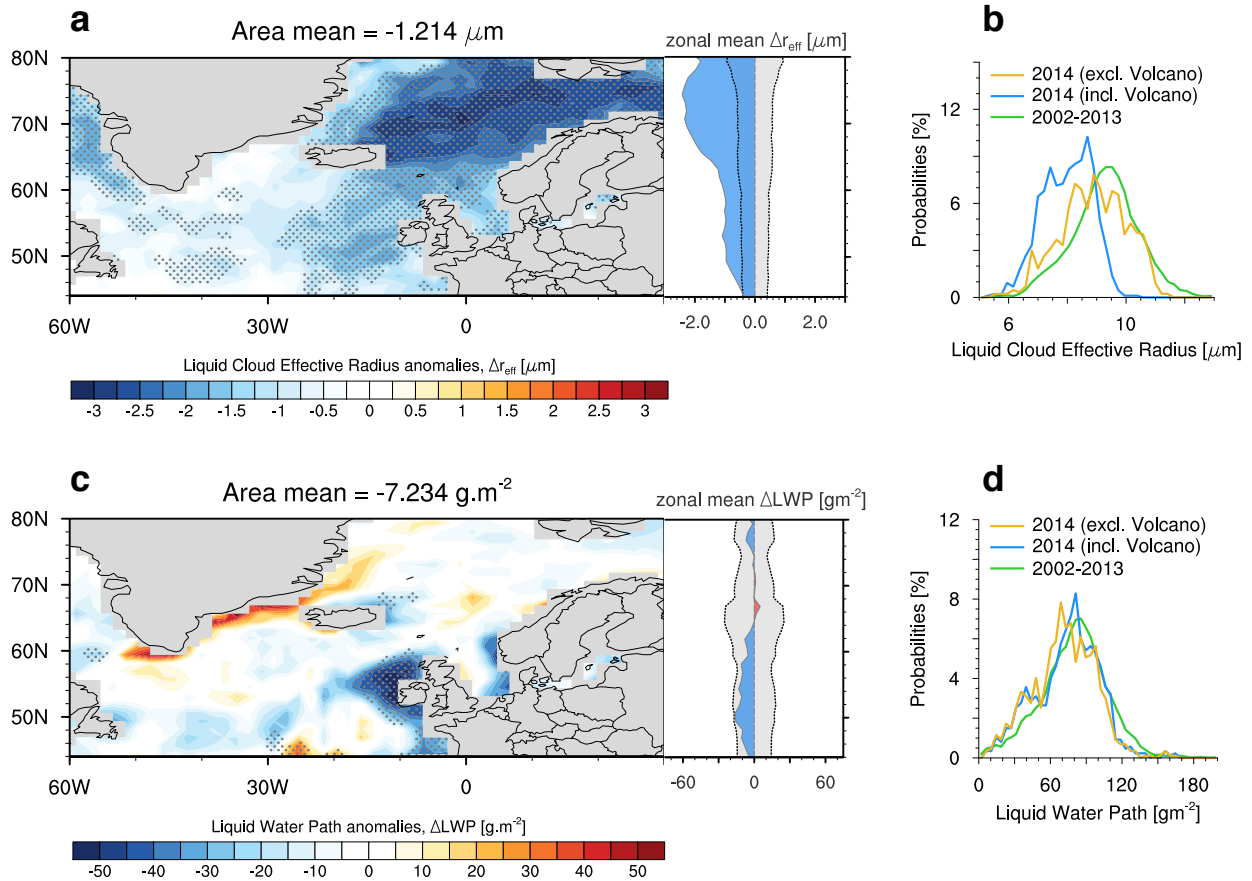
Figure S5.2. Changes in cloud properties as modelled by HadGEM3 using UKCA for September 2014.
The changes in (a) cloud droplet effective radius (μm) and (c) liquid water path (g.m⁻²) with corresponding zonal means attached. The probability distributions of absolute cloud droplet effective radius (b) and liquid water path (d) for the year 2014, including the Holuhraun emissions (blue), excluding the Holuhraun emissions (gold) and the 2002-2013 long-term mean (green). Stippling a) and c) represent areas where there is a significant perturbation at 95% confidence level based on a two-tailed Student's t-test. Grey shading in the zonal means represent the standard deviation over the 2002-2013 period.

S6. How do we know that perturbations are not driven by meteorological variability?

During September 2014, the meteorological reanalyses from NCEP (http://www.cpc.ncep.noaa.gov) shown in Figure S6.1a indicate a high pressure anomaly of 6-8 hPa centred to the north of Scotland and a low pressure anomaly of 6-8 hPa to the SW of the Bay of Biscay. This anomalous pressure pattern leads to anomalous easterly flow from the European continent which should increase N_d and decrease r_{eff} off the coast of the UK and northern Europe. During October 2014, a low pressure anomaly of 6-8 hPa exists to the NW of Scotland with a high pressure anomaly of around 8 hPa centred on Finland (Fig. S6.1b). The associated anomalous flow pattern is predominantly a southerly flow anomaly from the European continent. Examination of pressure patterns reveals that, for the period 2000-2015, the most similar meteorological conditions to September 2014 and October 2014 exist during September 2002 and October 2005, respectively. Figure S6.1c suggests that the anomalous flow pattern during September 2002 leads to anomalously low r_{eff} values in the North Atlantic off the coast of Europe, the UK and Ireland (Fig. S4.1 for MODIS). However, the spatial distribution of Δr_{eff} is of a far smaller spatial extent and lesser magnitude (-0.56 μm in 2002

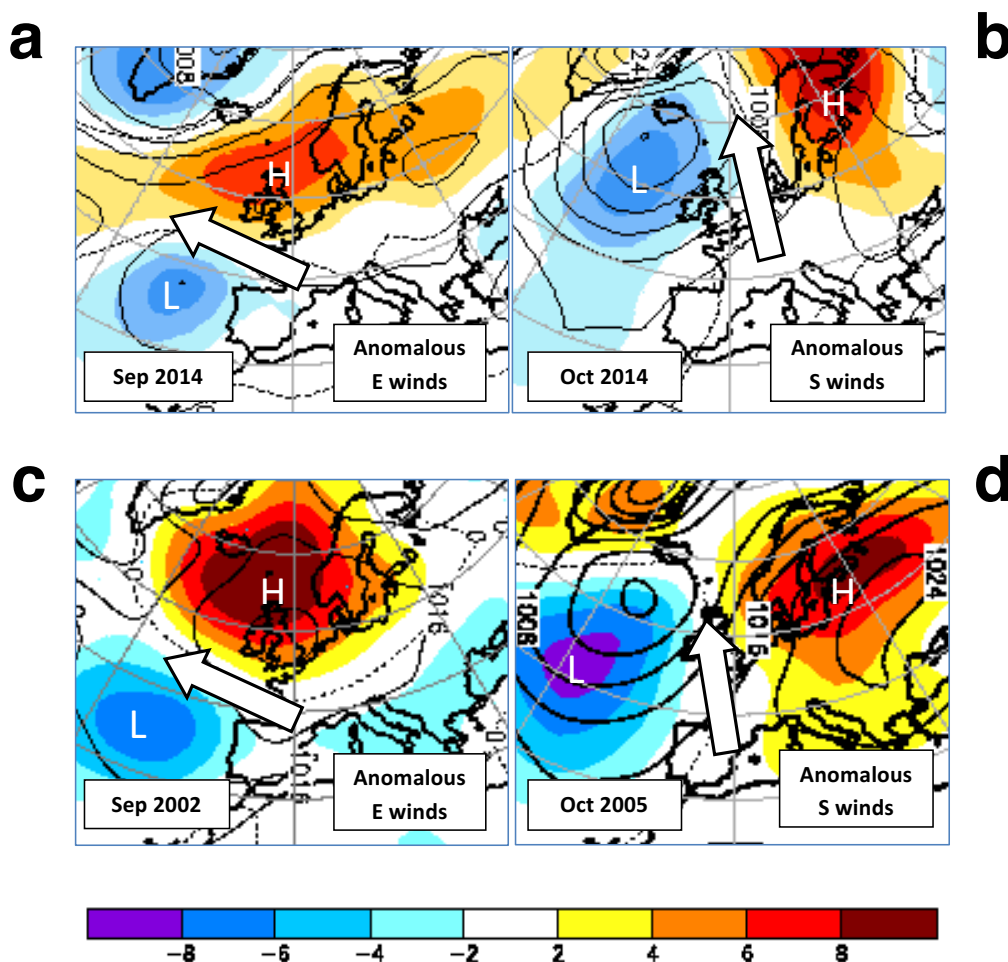***Figure S6.1. The large-scale meteorological conditions in the North Atlantic.*** *Showing the monthly mean sea level pressure (MSLP) in contours and the anomaly in MSLP with respect to the long-term mean in filled colours for September 2014 (a), October (2014), September 2002 (c) and October 2005 (d). The direction of anomalous flow off continental Europe is annotated in each case using an arrow. Units are hPa.*

compared to -0.98 μm in 2014 in the MODIS observations). Considering that Europe has reduced its emissions of PM2.5 pollutants and SO_2 by 60% and 80%, respectively, since 2002 (http://www.eea.europa.eu) and that these changes in emissions are accounted for in our model, meteorological variability can only account for a maximum of around 50% of the domain average Δr_{eff} in 2014.

Additional evidence that the meteorological impacts are a second-order impact is provided from modelling the effective radius perturbations for September (Fig. S4.3) and October (Fig. S4.4), with and without emissions from the 2014-15 eruption at Holuhraun. Our model simulations with/without the eruption for September 2014 suggest a domain-average Δr_{eff} of -1.21/-0.54 μm and for October 2014 suggest -0.68/-0.01 μm, respectively.

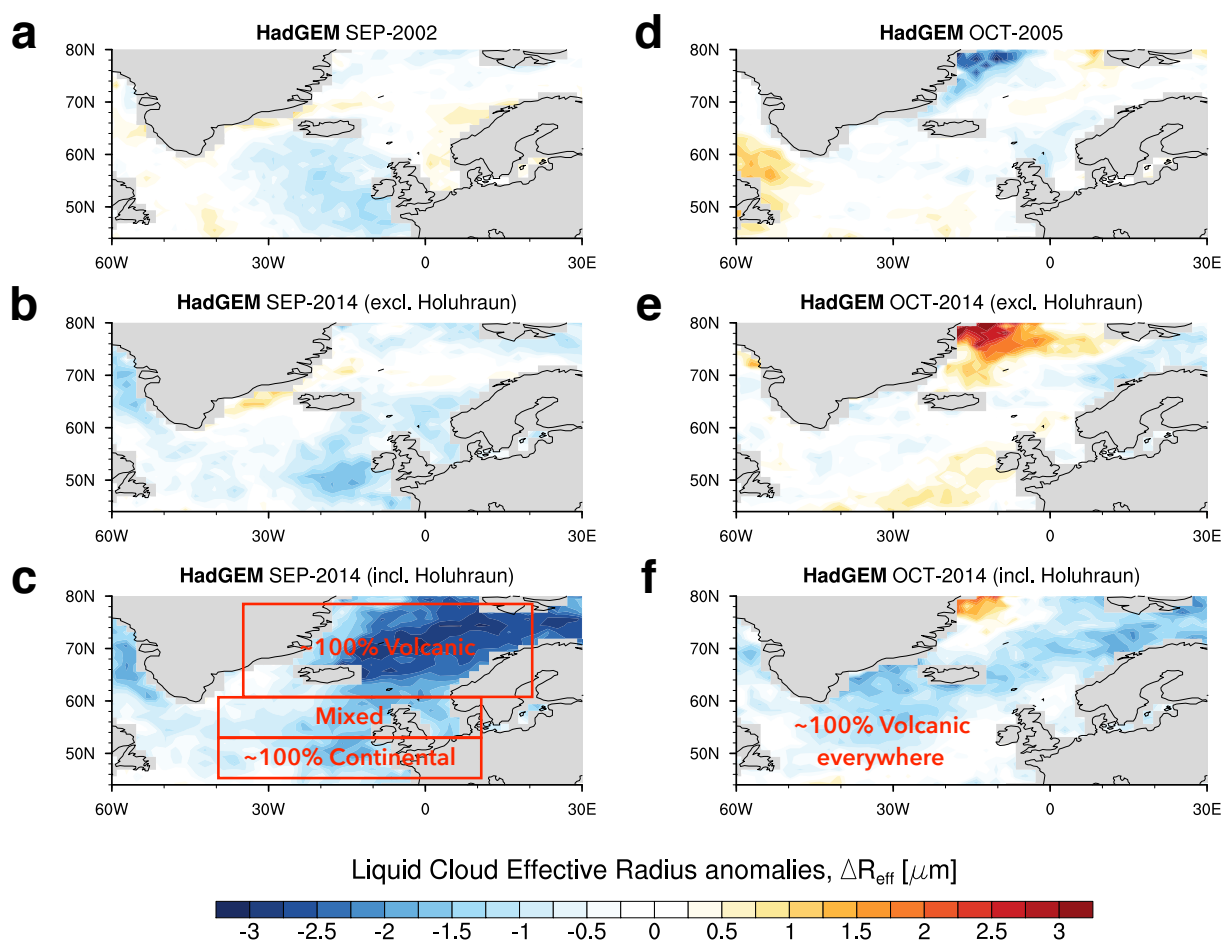Liquid Cloud Effective Radius anomalies, ΔR_{eff} [μm]

Figure S6.2. The influence of continental pollution on cloud effective radius anomalies. *HadGEM3 simulations showing Δr_{eff} (μm) for a) Sept 2002, b) Sept 2014 excluding the volcanic emissions, c) Sept 2014 including the volcanic emissions, d) Oct 2005, e) Oct 2014 excluding the volcanic emissions, f) Oct 2014 including the volcanic emissions.*

We examine the simulations with/without the volcanic eruption in more detail and compare the resulting Δr_{eff} to months with the most similar meteorology (Figure S6.2). The simulations including the emissions from Holuhraun in September 2014 show little impact on Δr_{eff} south of central Ireland indicating that Δr_{eff} in this region is likely caused by anthropogenic pollution in the model (and are

thus marked '~100% Continental'), while Δr_{eff} in areas between central Ireland and Iceland are due to a combination of continental and volcanic emissions (and are thus marked 'Mixed'). Elsewhere, Δr_{eff} in the model simulations are due to volcanic emissions. Note that comparing this assessment against Figure S5.2 reveals that 95% confidence appears a reasonably stringent metric for removing meteorological variability in Δr_{eff}. This is because the 95% confidence level appears to distinguish those points to the north of central Ireland which are affected by both volcanic and continental emissions from those to the south of central Ireland which are ~100% continental in origin.

The situation for October 2014 appears more clear-cut. October 2005 shows some systematic Δr_{eff} to the north of Scandinavia (Fig. S6.2d), but in 2014 the Δr_{eff} without volcanic emissions is generally small (Fig. S6.2e), with an average of -0.01 µm over the domain in the simulations. The simulations including emissions from the eruption reveal an extensive large perturbation across the entire North Atlantic of -0.68 µm, thus the impact appears to be ~100% volcanic across the domain.

S7. On the detectability of Δr_{eff}, ΔN_d, ΔLWP, $\Delta \tau_{cloud}$, and ΔTOA_{SW}

A simple theoretical framework[37] is that the properties of *a* cloud, *c*, are a function of the meteorology, *m*, and the aerosol, *a*, *c(m,a)*. Neglecting the interdependency between *m* and *a*, then,

$$\delta c = \frac{\partial c}{\partial m}\delta m + \frac{\partial c}{\partial a}\delta a$$

We are able to isolate the impacts of aerosol and meteorology by comparing model simulations which include and exclude the emissions from Holuhraun during 2014 ($HOL_{2014} - NO\_HOL_{2014}$) and also model simulations of 2014 compared to those for 2002-2013 ($HOL_{2014} - NO\_HOL_{2002-2013}$).

S7.1. Detectability of Δr_{eff}

For r_{eff},

$$\delta r_{eff} = \frac{\partial r_{eff}}{\partial m}\delta m + \frac{\partial r_{eff}}{\partial a}\delta a$$

Simulations of $HOL_{2014} - NO\_HOL_{2014}$ using a nudged model force μm to be small, yielding,

$$\delta r_{eff} \approx \frac{\partial r_{eff}}{\partial a}\delta a$$

The $HOL_{2014} - NO\_HOL_{2002-2014}$ difference removes the constraints on meteorology, but yields a similar result to the simulations using 2014 meteorology with and without the eruption (i.e. $HOL_{2014} - NO\_HOL_{2014}$) suggesting that the term $(\partial r_{eff}/\partial m)\delta m$ is small reaffirming that the impact of meteorology on r_{eff} is small. The exception to this is to the south of the region for September where the contribution to the zonal mean Δr_{eff} is larger from the meteorological variability than from the aerosol injection (Fig. S7.1a and c), supporting our inference that this is due to the meteorological impact from anomalous easterly flow (section S6). Thus, for large perturbations to the aerosol, it should be relatively easy to observe $(\partial r_{eff}/\partial a)\delta a$ (or the 'first' indirect effect) as evident in the MODIS retrievals.

S7.2. Detectability of ΔN_d

For N_d,

$$\delta N_d = \frac{\partial N_d}{\partial m}\delta m + \frac{\partial N_d}{\partial a}\delta a$$

The comparison between ΔN_d from MODIS and HadGEM3 again reveals a reasonable spatial distribution for September and October 2014 (Figure S7.2a, b, g and h), and again indicates the influence of anomalous easterly winds bringing polluted air off the European continent in the south of the region for September 2014 (Figure S7.2e and f). For September, the model tends to rather over-predict ΔN_d in the volcano-influenced region while for October there appears to be an under prediction, findings that are consistent with the over- and under- prediction of Δr_{eff} noted in section S7.1.

S7.3. Detectability of of ΔLWP

For LWP,

$$\delta LWP = \frac{\partial LWP}{\partial m}\delta m + \frac{\partial LWP}{\partial a}\delta a$$

Again, simulations of $HOL_{2014}-NO\_HOL_{2014}$ using a nudged model and the same meteorology force δm to be small, yielding,

$$\delta LWP \approx \frac{\partial LWP}{\partial a}\delta a$$

or the 'second' indirect effect. Simulations of $HOL_{2014}-NO\_HOL_{2002-2013}$, remove the constraints on meteorology, but this time yield very different results suggesting that the term $(\partial LWP/\partial m)\delta m$ is large compared to $(\partial LWP/\partial a)\delta a$. Thus, it is unlikely that $\partial LWP/\partial a$ will be detectable from monthly mean observations.

S7.4. Detectability of Δτ_cloud

For τ_{cloud}, noting equation (1), main text, and that the terms $(\partial reff/\partial m)\delta m$ and $(\partial LWP/\partial a)\delta a$ are small,

$$\delta \tau_{cloud} = \frac{\partial \tau_{cloud}}{\partial m}\delta m + \frac{\partial \tau_{cloud}}{\partial a}\delta a$$

The model simulations shown in Figure S7.4 suggests that the change in τ_{cloud} in the model is dominated by the $(\partial \tau_{cloud}/\partial a)\delta a$ term and that an impact on τ_{cloud} should be detectable in observations above the meteorological variability provided the model represents observed variability reasonably. This is seen to be the case as there is a strong coherence between Figure 7.4c and 7.4g and 7.4d and 7.4h respectively.

S7.5. Detectability of ΔToA_{SW}

While Δr_{eff} and $\Delta \tau_{cloud}$ are detectable in the model, ultimately it is the radiative forcing from the volcanic eruption that is of most relevance to climate. We investigate the radiative forcing in the SW region of the spectrum first. While the top of atmosphere shortwave radiative forcing (ΔToA_{SW}) is influenced by changes in τ_{cloud}, it will also be influenced by the seasonal cycle of solar insolation and other factors that scatter and absorb solar radiation such as aerosols and water vapour. Nevertheless, a similar analysis is performed to determine the spatial distribution and magnitude of the influence from aerosol-cloud-interactions and meteorological variability,

$$\delta ToA_{SW} = \frac{\partial ToA_{SW}}{\partial m}\delta m + \frac{\partial ToA_{SW}}{\partial a}\delta a$$

The Clouds and the Earth's Radiant Energy System (CERES, https://ceres.larc.nasa.gov/) sensor provides top of atmosphere (ToA) shortwave (SW) fluxes for the period 2000-2015, and we provide estimates of the impact on ToA$_{SW}$ impact by examining the difference between the ToA SW flux in 2014 from the long-term (2002-2013) mean for both CERES and HadGEM3.

The model and the observations show ΔToA_{SW} of up to -15 W.m^{-2} across large areas of the domain in coherent patterns. While there are similarities in the position of ΔToA_{SW} when compared to τ_{cloud}, the largest perturbations are shifted to the south particularly for October, consistent with the solar insolation. The agreement between the model and the observations gives us confidence that the model is representing reality with reasonable fidelity.

The zonal mean perturbations show a reasonable degree of coherence when the volcanic eruptions are included which is not evident when the volcano is absent from the simulations. The impacts of meteorology (Figures S7.5e,f) introduce 'noise' to the system, and generally act in the opposite sense to the influence of the volcano (zonal plots in Figures S7.5a,b). That there is little spatial coherence between Fig. S7.5e and Fig. S7.5g but reasonable coherence between Fig. S7.5c and Fig. S7.5g, particularly northward of 55°N, where aerosol optical depths are significantly perturbed by the volcanic eruption suggests that the signal is robust.

The effective radiative forcing (derived from parallel model simulations including and excluding the eruption and calculated for both SW and LW radiation) from the model for September-October is around -3 W.m^{-2} over ocean over the region of investigation. The global mean radiative forcing is -0.21 W.m^{-2} for September-October or an annual mean radiative forcing of around -0.04 W.m^{-2} assuming that there was no impact outside of September-October 2014. This estimate is likely a lowest estimate as there may be impacts in other months.
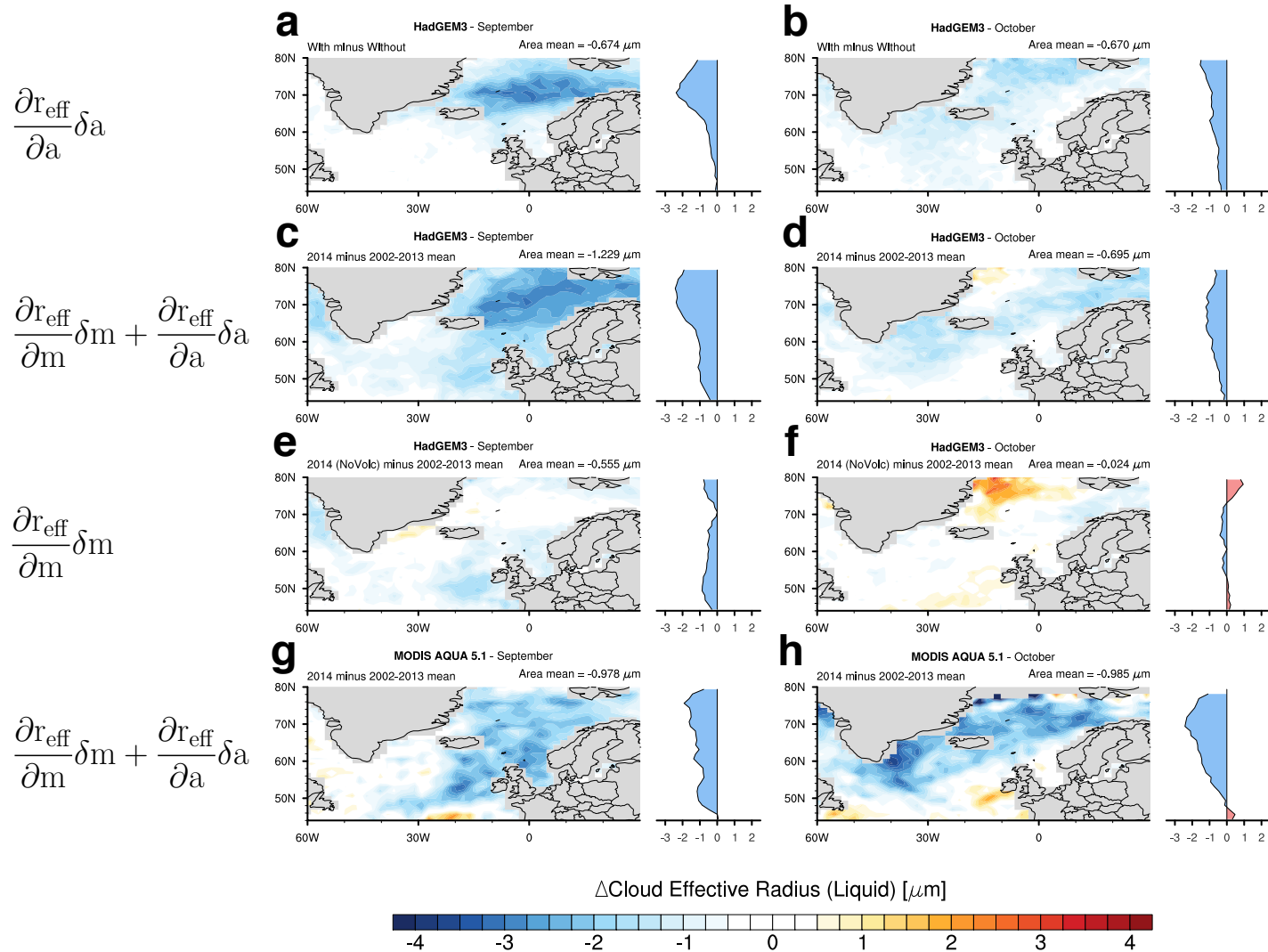
$$\frac{\partial r_{eff}}{\partial a}\delta a$$

$$\frac{\partial r_{eff}}{\partial m}\delta m + \frac{\partial r_{eff}}{\partial a}\delta a$$

$$\frac{\partial r_{eff}}{\partial m}\delta m$$

$$\frac{\partial r_{eff}}{\partial m}\delta m + \frac{\partial r_{eff}}{\partial a}\delta a$$

Figure S7.1. The effect of Meteorology and Aerosols on effective radius anomalies. *Showing Δr_{eff} (μm) from HadGEM3 for a) September and b) October using the $HOL_{2014}−NO\_HOL_{2014}$ simulations, c) September and d) October using the $HOL_{2014}−NO\_HOL_{2002-2013}$ simulations, e) September and f) October using the $NO\_HOL_{2014}−NO\_HOL_{2002-2013}$ simulations. g) and h) show the corresponding analyses for AQUA MODIS. The panels to the right of each map show the zonal mean over the domain.*

$$\frac{\partial N_d}{\partial a}\delta a$$

$$\frac{\partial N_d}{\partial m}\delta m + \frac{\partial N_d}{\partial a}\delta a$$

$$\frac{\partial N_d}{\partial m}\delta m$$

$$\frac{\partial N_d}{\partial m}\delta m + \frac{\partial N_d}{\partial a}\delta a$$

Figure S7.2. The effect of Meteorology and Aerosols on N_d anomalies. Showing ΔN_d *(cm⁻³) from HadGEM3 for a) September and b) October using the HOL_{2014}−NO_HOL_{2014} simulations, c) September and d) October using the HOL_{2014}−NO_HOL_{2002−2013} simulations, e) September and f) October using the NO_HOL_{2014}−NO_HOL_{2002−2013} simulations. g) and h) show the corresponding analyses for AQUA MODIS. The panels to the right of each map show the zonal mean over the domain.*
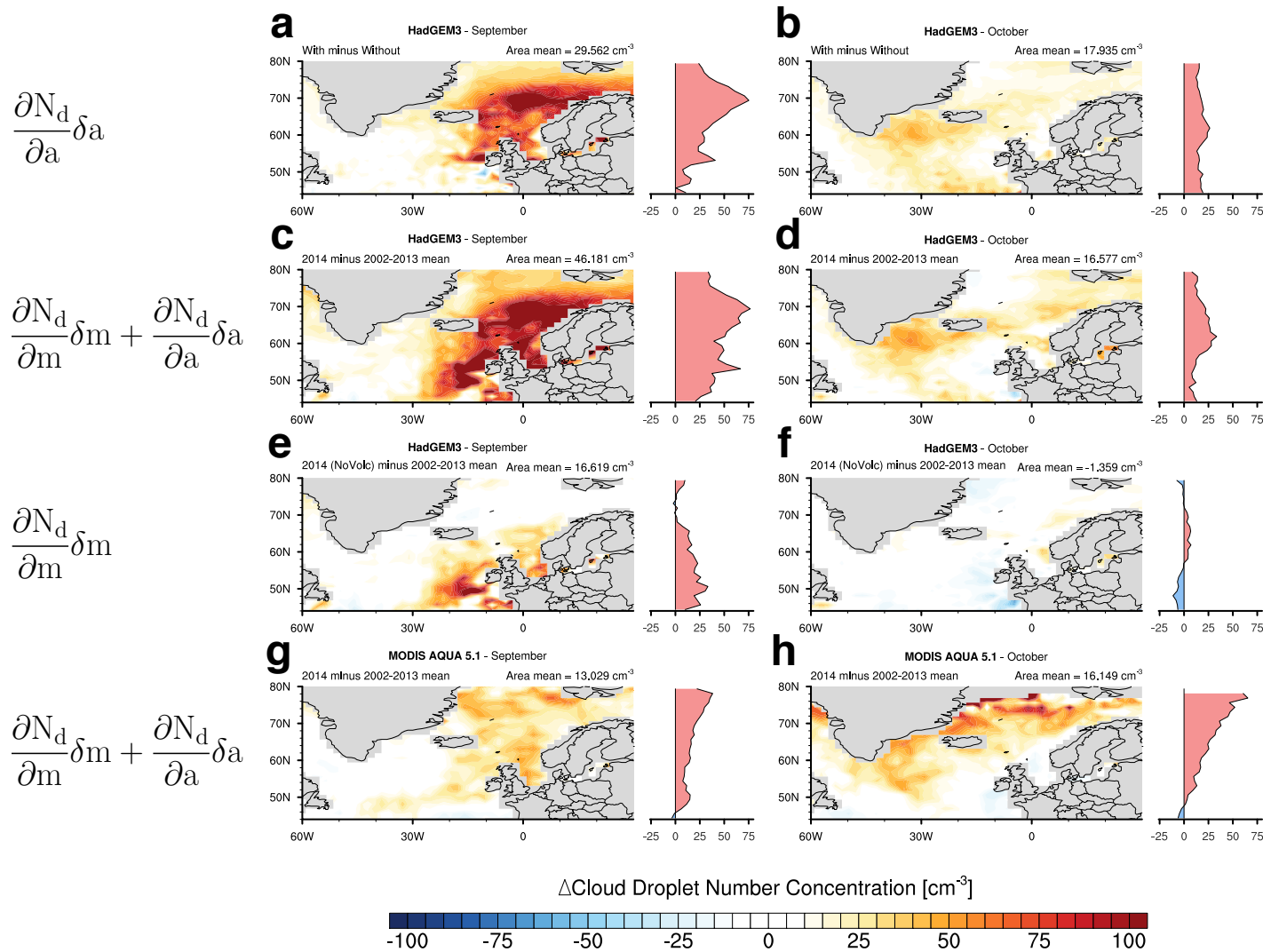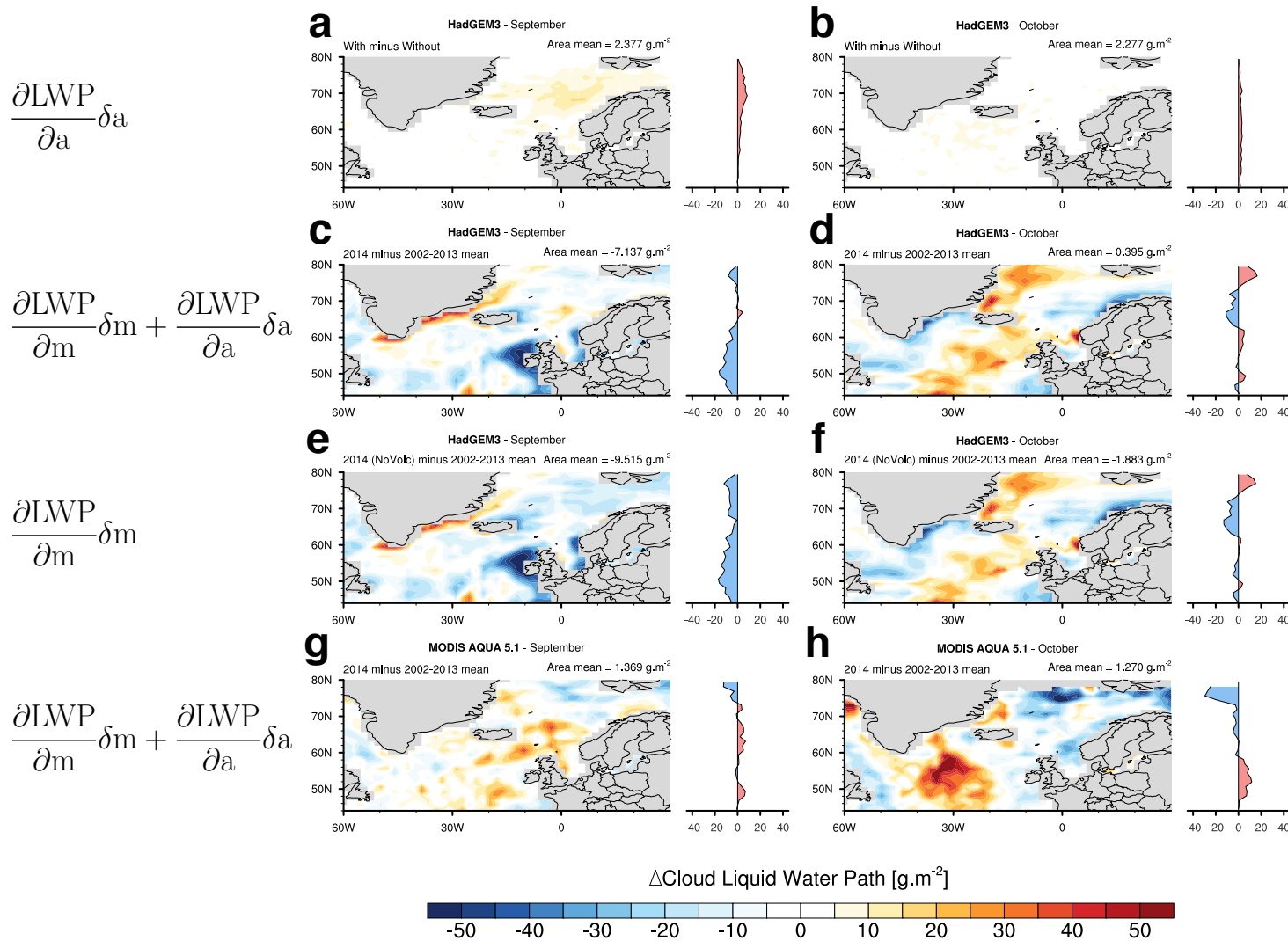
$$\frac{\partial \text{LWP}}{\partial a}\delta a$$

$$\frac{\partial \text{LWP}}{\partial m}\delta m + \frac{\partial \text{LWP}}{\partial a}\delta a$$

$$\frac{\partial \text{LWP}}{\partial m}\delta m$$

$$\frac{\partial \text{LWP}}{\partial m}\delta m + \frac{\partial \text{LWP}}{\partial a}\delta a$$

a HadGEM3 - September
With minus Without   Area mean = 2.377 g.m^{-2}

b HadGEM3 - October
With minus Without   Area mean = 2.277 g.m^{-2}

c HadGEM3 - September
2014 minus 2002-2013 mean   Area mean = -7.137 g.m^{-2}

d HadGEM3 - October
2014 minus 2002-2013 mean   Area mean = 0.395 g.m^{-2}

e HadGEM3 - September
2014 (NoVolc) minus 2002-2013 mean   Area mean = -9.515 g.m^{-2}

f HadGEM3 - October
2014 (NoVolc) minus 2002-2013 mean   Area mean = -1.883 g.m^{-2}

g MODIS AQUA 5.1 - September
2014 minus 2002-2013 mean   Area mean = 1.369 g.m^{-2}

h MODIS AQUA 5.1 - October
2014 minus 2002-2013 mean   Area mean = 1.270 g.m^{-2}

$\triangle$Cloud Liquid Water Path [g.m^{-2}]

Figure S7.3. The effect of Meteorology and Aerosols on LWP anomalies. Showing ΔLWP (g.m^{-2}) from HadGEM3 for a) September and b) October using the HOL$_{2014}$−NO_HOL$_{2014}$ simulations, c) September and d) October using the HOL$_{2014}$−NO_HOL$_{2002-2013}$ simulations, e) September and f) October using the NO_HOL$_{2014}$−NO_HOL$_{2002-2013}$ simulations. g) and h) show the corresponding analyses for AQUA MODIS. The panels to the right of each map show the zonal mean over the domain.
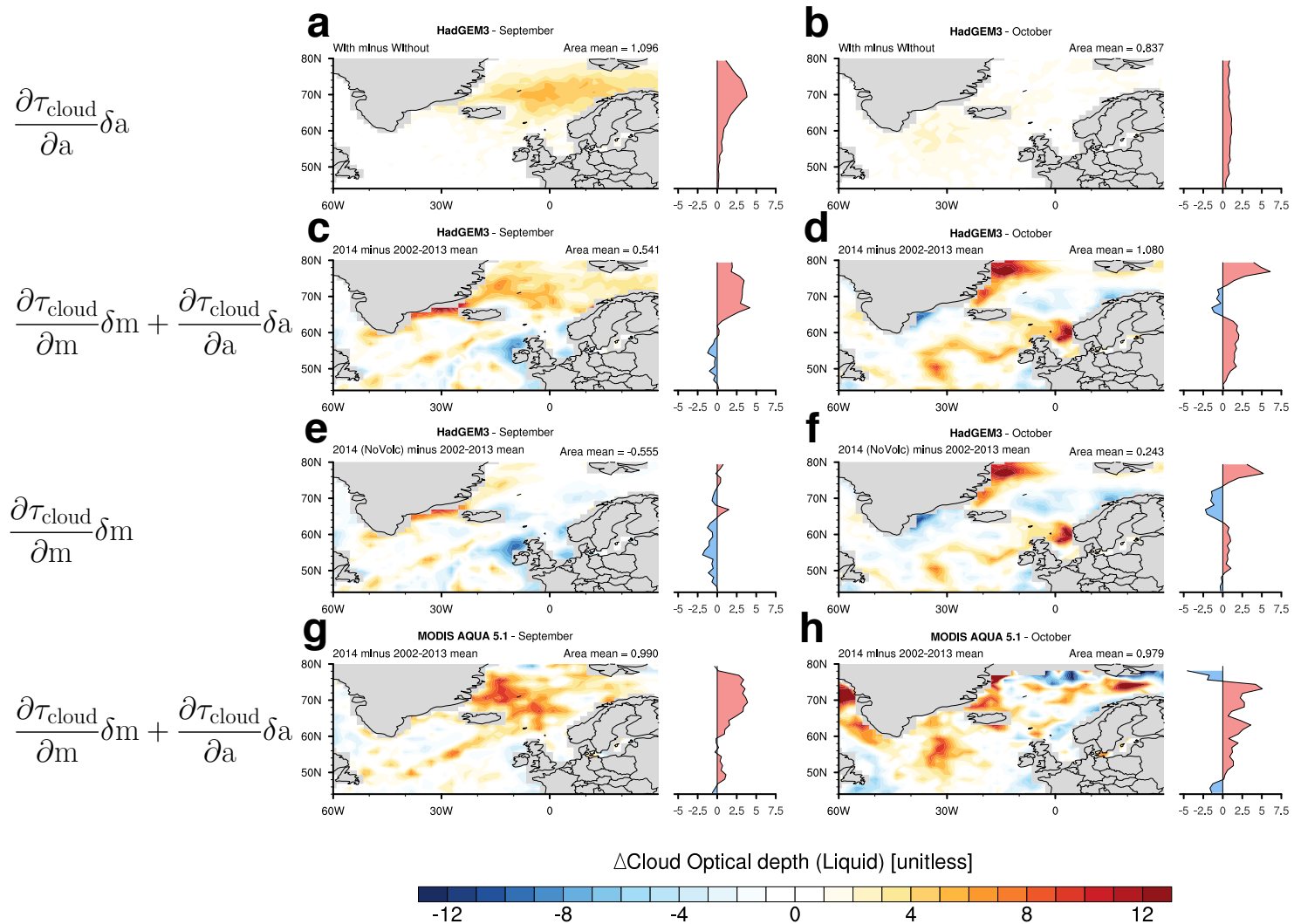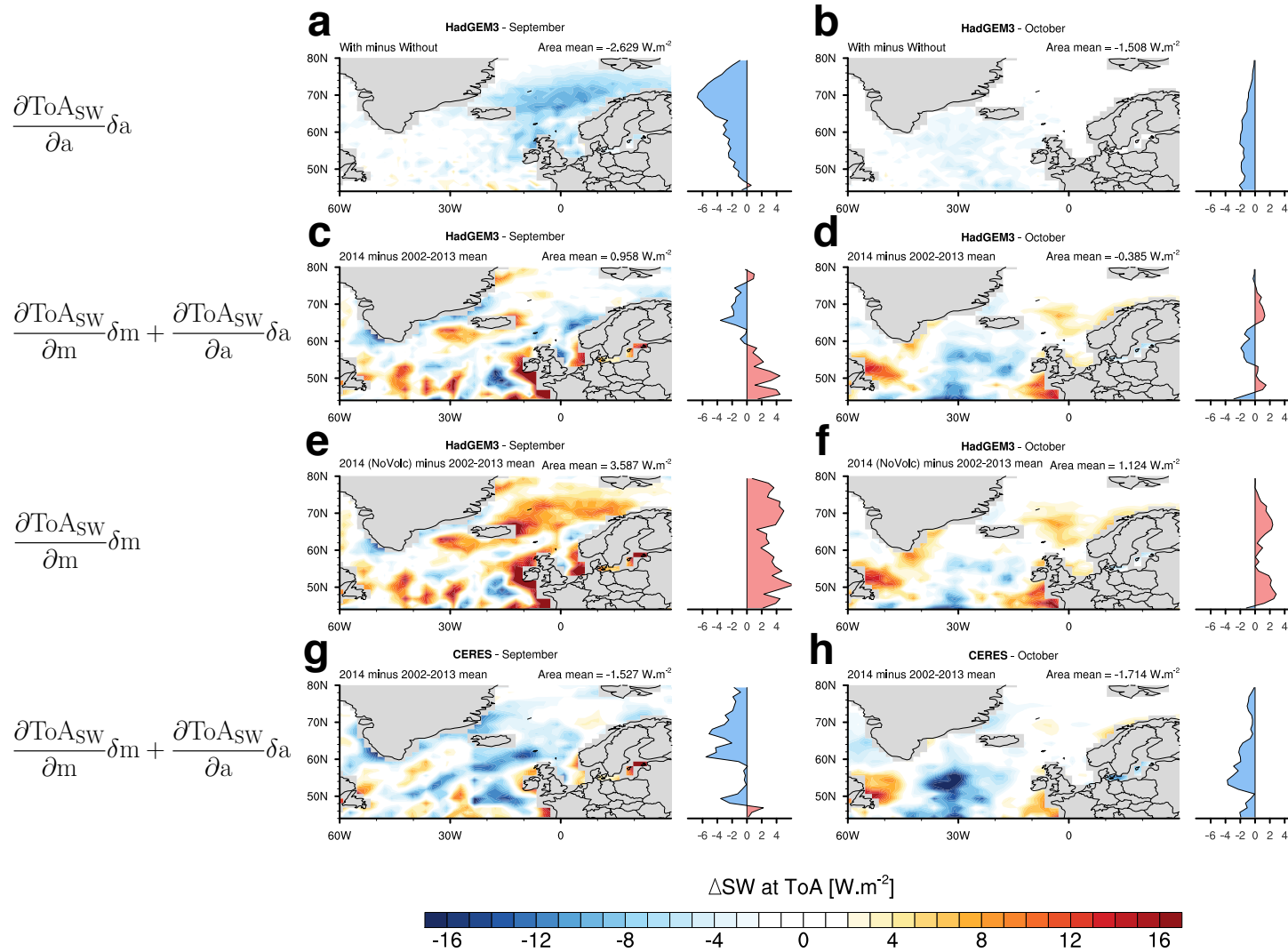
Figure S7.4. The effect of Meteorology and Aerosols on cloud optical depth anomalies. *Showing $\Delta\tau_{cloud}$ (unitless) from HadGEM3 for a) September and b) October using the $HOL_{2014}-NO\_HOL_{2014}$ simulations, c) September and d) October using the $HOL_{2014}-NO\_HOL_{2002-2013}$ simulations, e) September and f) October using the $NO\_HOL_{2014}-NO\_HOL_{2002-2013}$ simulations. g) and h) show the corresponding analyses for AQUA MODIS. The panels to the right of each map show the zonal mean over the domain.*

$$\frac{\partial \text{ToA}_{\text{SW}}}{\partial a}\delta a$$

$$\frac{\partial \text{ToA}_{\text{SW}}}{\partial m}\delta m + \frac{\partial \text{ToA}_{\text{SW}}}{\partial a}\delta a$$

$$\frac{\partial \text{ToA}_{\text{SW}}}{\partial m}\delta m$$

$$\frac{\partial \text{ToA}_{\text{SW}}}{\partial m}\delta m + \frac{\partial \text{ToA}_{\text{SW}}}{\partial a}\delta a$$

Figure S7.5. The effect of Meteorology and Aerosols on Top of the Atmosphere Short Wave anomalies. Showing ΔToA_{SW} (W.m^{-2}) from HadGEM3 for a) September and b) October using the HOL$_{2014}$−NO_HOL$_{2014}$ simulations, c) September and d) October using the HOL$_{2014}$−NO_HOL$_{2002-2013}$ simulations, e) September and f) October using the NO_HOL$_{2014}$−NO_HOL$_{2002-2013}$ simulations. g) and h) show the corresponding analyses for AQUA MODIS. The panels to the right of each map show the zonal mean over the domain.

S8. Examining the multi-model performance for September 2014

As for October 2014, Figure S8.1 shows the same general features are present in September 2014; Δr_{eff} is well represented by HadGEM3 using UKCA, CAM5-NCAR, and CAM5-Oslo, but HadGEM3-CLASSIC produces too large a change when compared to the MODIS retrievals. The ΔLWP in CAM5-NCAR (>18 g.m^{-2}) is not supported by MODIS where the 2002-2013 domain-mean standard deviation in ΔLWP for September is 3.1 g.m^{-2}.
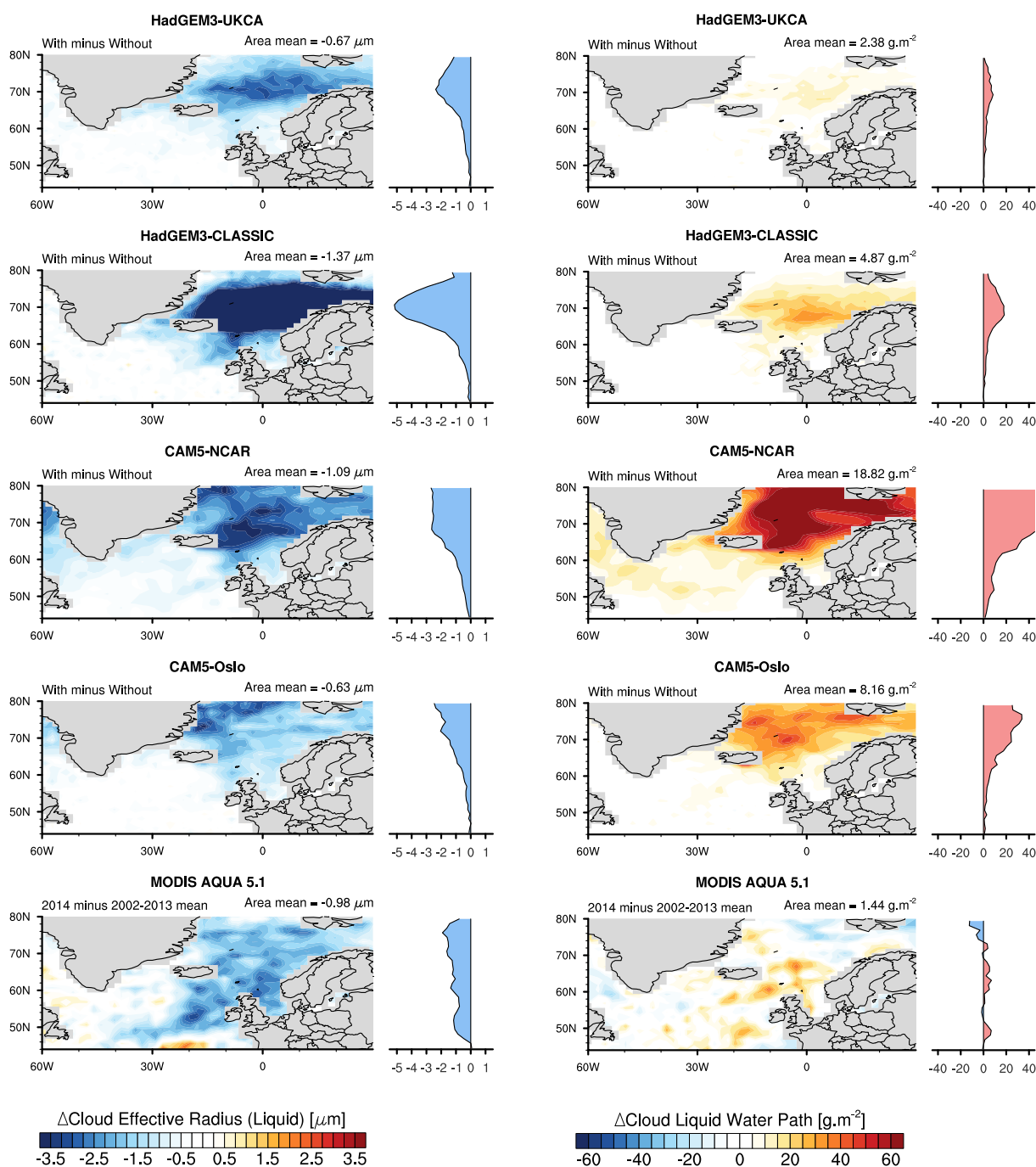
Figure S8.1. Multi-model estimates of the changes in cloud properties for September 2014. *Left column shows Δr$_{eff}$ (µm) and right column ΔLWP (g.m^{-2}) determined from HadGEM3 using the 2-moment UKCA/ GLOMAP-mode aerosol scheme (first row), HadGEM3 using the single moment CLASSIC aerosol scheme (second row) CAM5-NCAR (third row), CAM5-Oslo (fourth row) and AQUA MODIS (last row). Note that MODIS anomalies show the aerosol impacts plus the meteorological variability while the model simulations show the impact of aerosols only.*

S9. Influence of the aerosol scheme on the model responses

HadGEM3-CLASSIC is a single moment aerosol scheme and therefore any increase in aerosol mass concentration necessarily leads to an increase in aerosol number and thus in the number of cloud droplets, N_d, via an empirical relationship between N_d and cloud condensation nuclei[65].

Figure S9.1 shows that the response of HadGEM3 using UKCA is clearly reduced compared to HadGEM3-CLASSIC. This is one of the main motivations for implementing a more advanced double moment (i.e. mass and number) aerosol scheme in HadGEM3; while the aerosol-radiation interactions can be reasonably represented using CLASSIC, aerosol-cloud interactions require a more sophisticated treatment to include impacts on the aerosol size distribution.
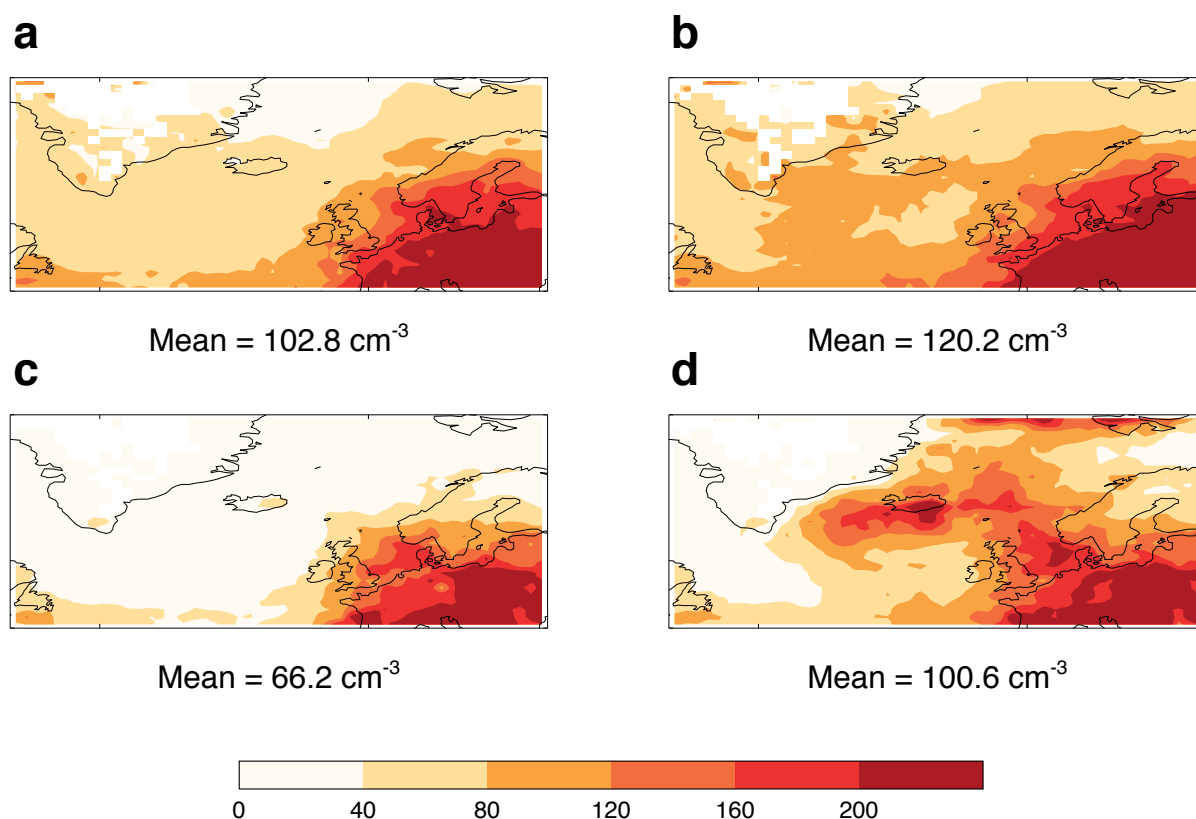
Figure S9.1. The differences in modelled N_d between HadGEM3 two aerosol schemes. *Showing the cloud droplet number concentration (N_d, cm^{-3}) for a) HadGEM3 using UKCA excluding the eruption, b) HadGEM3 using UKCA including the eruption, c) HadGEM3-CLASSIC excluding the eruption, d) HadGEM3-CLASSIC including the eruption.*

S10. Precipitation patterns during September/October 2014

If clouds were not precipitating during the period of the event, any aerosol perturbations, even a huge one such as the 2014-15 eruption at Holuhraun, cannot make the clouds precipitate less. However, the figure S10.1 shows that, on the contrary *i*) 2014 is not an anomalously dry year and *ii*) that precipitations during the period of interested (SEP-OCT) are far from being low (~4 mm/day). Therefore, it is reasonable to expect precipitating clouds to be present in the studied region during the 2014-15 Holuhraun eruption.

To further illustrate the absence of an impact on precipitation, we show the year by year analysis of the GPCP (https://www.esrl.noaa.gov/psd/data/gridded/data.gpcp.html) precipitation anomalies (Figure S10.2 and S10.3). The main conclusion here is that precipitation is not altered during 2014 which supports the idea that despite a strong aerosol perturbation, cloud systems overcome any
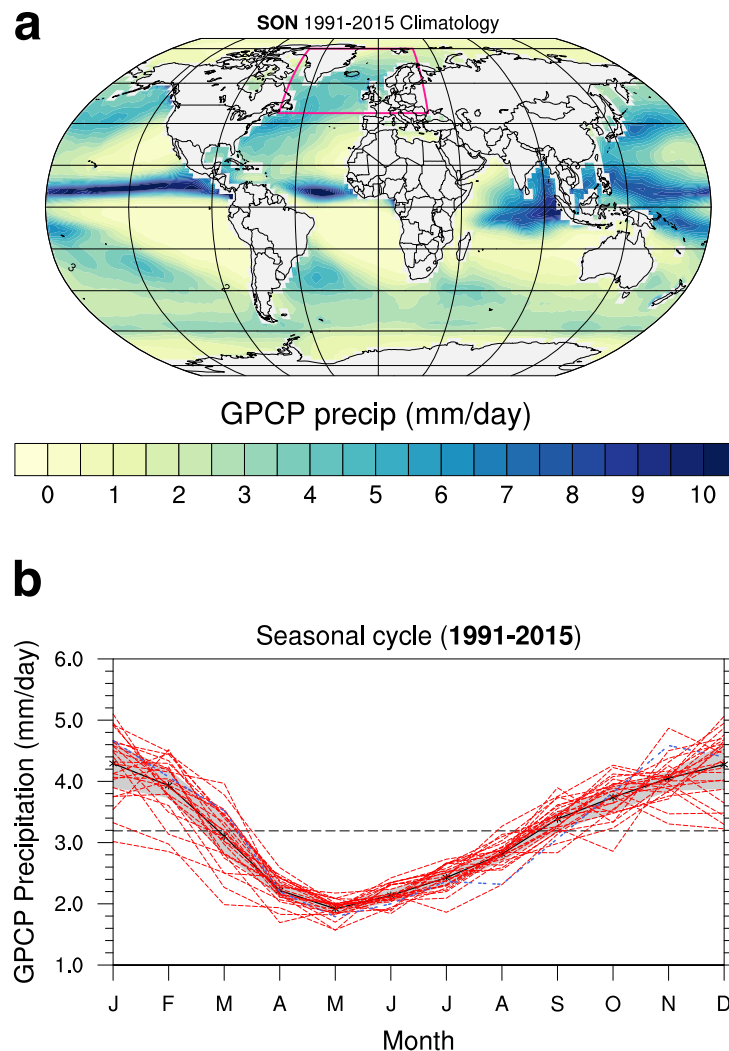

Figure S10.1. The climatology of surface precipitation from GPCP. *The precipitation rate (in mm/day) shown as a) September-October-November (SON) seasonal average for the 1991-2015 period, and b) the corresponding seasonal cycle derived for the region in the vicinity of Holuhraun (45°N-80°N; 60°E-30°W). The long term (1991-2015) mean seasonal cycle is represented by the black line. The red dashed lines represent the seasonal cycle for each individual year. 2014 is highlighted in blue.*

microphysical perturbations and readjust to a new equilibrium where neither LWP or precipitation are significantly perturbed.

Figure S10.4 shows precipitation from the run including the eruption for the three models and the GPCP observations. Modelled precipitation is all in very good agreement between the three models and matches reasonably well the observed GPCP precipitations. The fact that models exhibit precipitation suggests that the autoconversion process will likely play a role in modulating the cloud LWP response. Therefore, an alternative way of assessing the impact of the second indirect effects is also considered by assessing the impacts of running the models with and without impacts beyond the first indirect effect. This is performed by turning off any impact of the change in the effective radius on the auto-conversion scheme in each model. Note that both the HadGEM3 model and the CAM5-Oslo model have prognostic cloud/prognostic condensate schemes. All models use the Khairoutdinov and Kogan scheme[55]. CAM5-Oslo, uses the same subgrid-scale amplification in the autoconversion process[66] as in CAM5-NCAR; HadGEM3 using UKCA too has a similar representation[67]. The results show the relative importance of the life-time effects for each of the GCMs (Figures S10.5). HadGEM3 using UKCA shows only a small difference in LWP between the STAN simulations and those with no sensitivity of auto-conversion to aerosol concentration ('No-Life' experiments). CAM5-NCAR shows the largest difference and CAM5-Oslo an intermediate response.

It is acknowledged that detailed process-level understanding is required to fully explain all model differences. Systematic investigations would need to consider processes beyond just microphysics parametrisation, in particular the cloud fraction scheme, the parametrised critical relative humidity and the simulated relative humidity from each model. While such an investigation is important, it is beyond the scope of the present work.
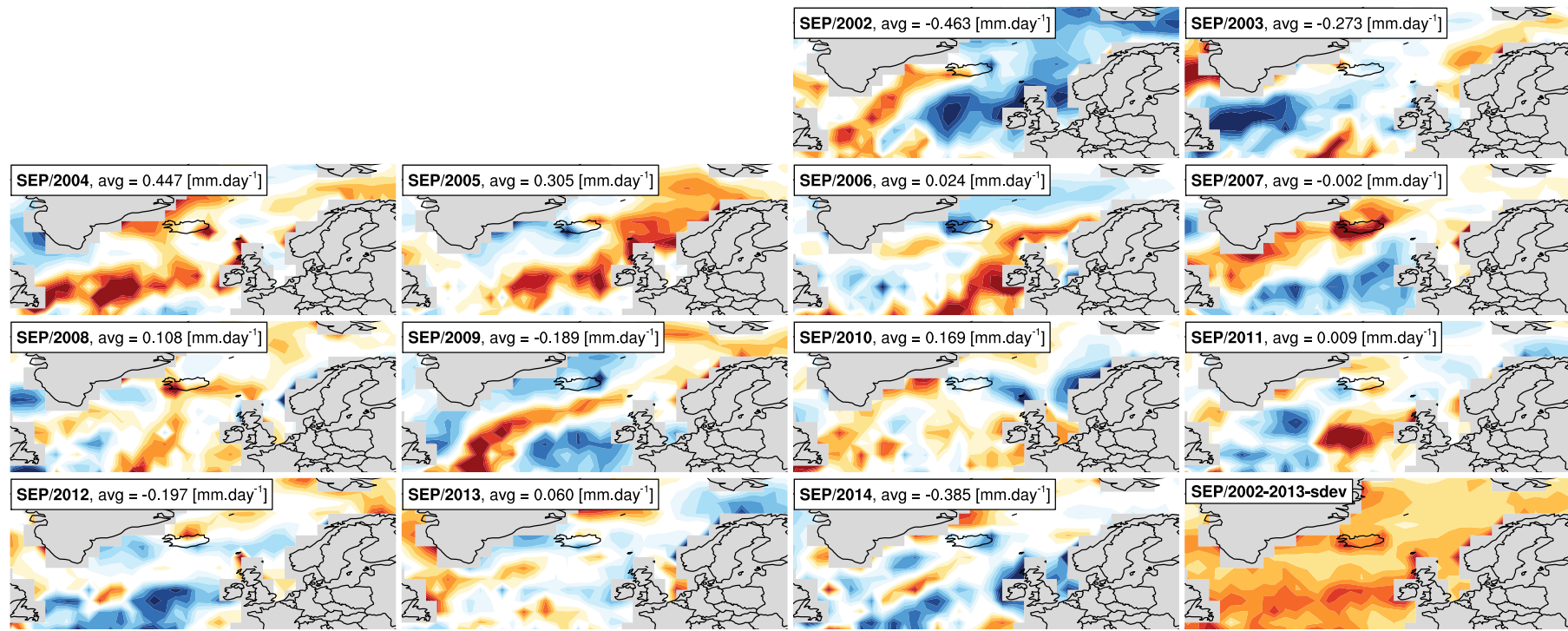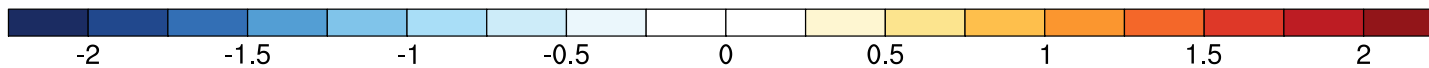
Figure S10.2. **The precipitation rate anomalies during September months from GPCP**. *The precipitation rate anomalies are shown from 2002 to 2014 period (in mm/day) with their associated zonal mean (continued). The anomalies are calculated with regard to the 2002-2013 climatology. The grey shading represents the standard deviation from the 2002-2013 period. The last panel shows the precipitation rate standard deviation (sdev) calculated for the 2002-2013 period. In the first 13 panels, 'avg' represents the average anomalies.*
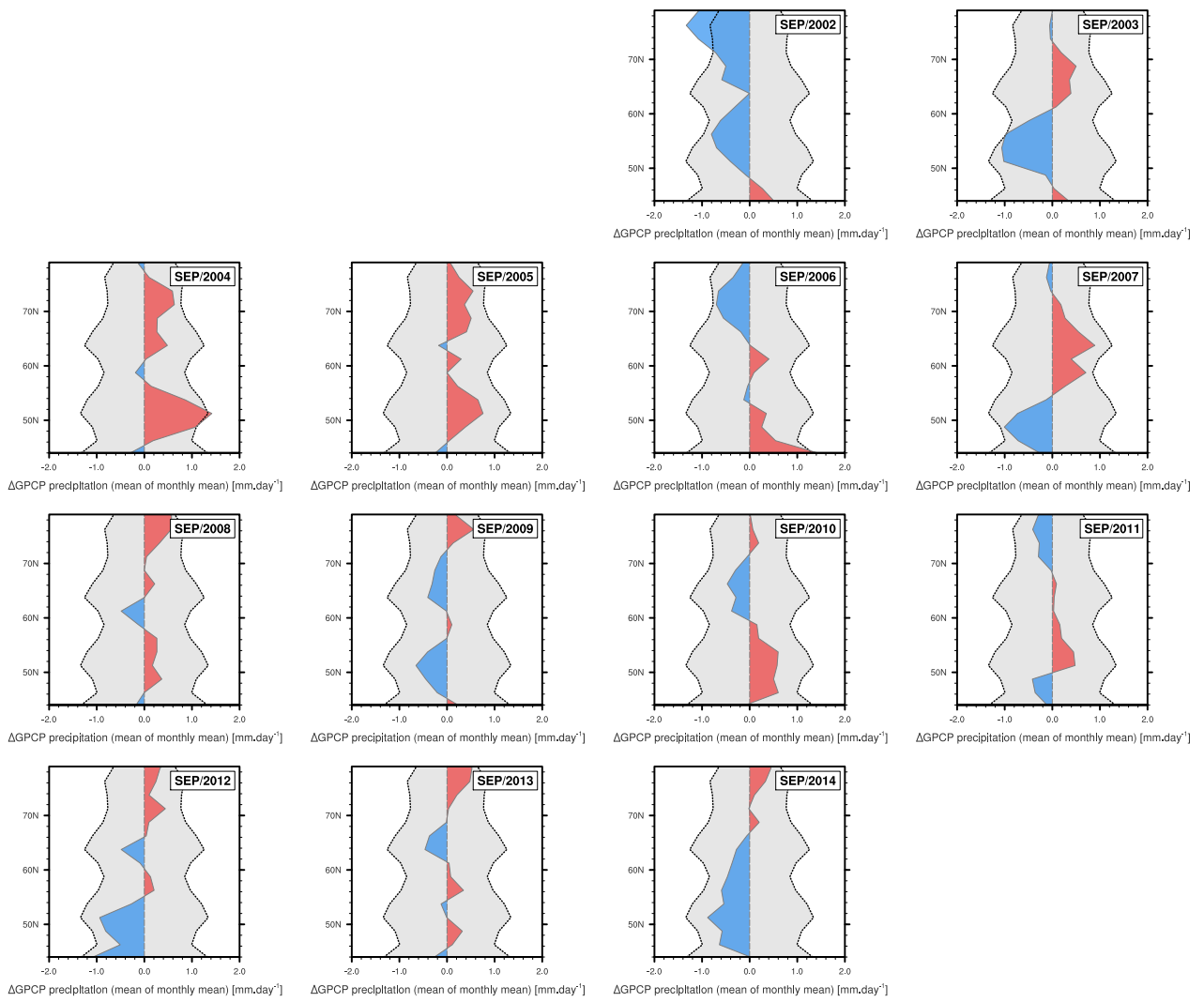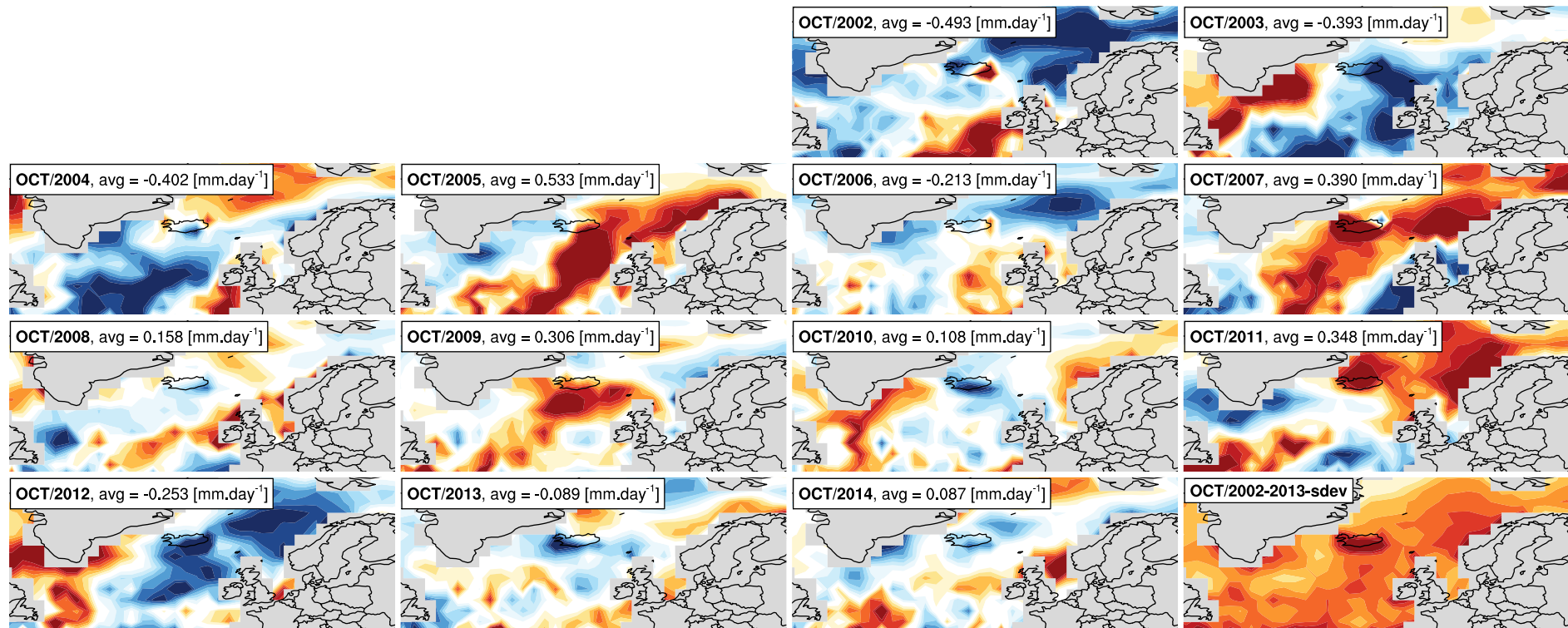
Each panel caption / axis label: ΔGPCP precipitation (mean of monthly mean) [mm.day⁻¹]

Panels labeled: SEP/2002, SEP/2003, SEP/2004, SEP/2005, SEP/2006, SEP/2007, SEP/2008, SEP/2009, SEP/2010, SEP/2011, SEP/2012, SEP/2013, SEP/2014
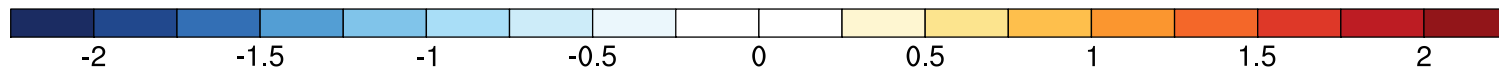
Figure S10.2. continued

Figure S10.3. **The precipitation rate anomalies during October months from GPCP.** *The precipitation rate anomalies are shown from 2002 to 2014 period (in mm/day) with their associated zonal mean (continued). The anomalies are calculated with regard to the 2002-2013 climatology. The grey shading represents the standard deviation from the 2002-2013 period. The last panel shows the precipitation rate standard deviation (sdev) calculated for the 2002-2013 period. In the first 13 panels, 'avg' represents the average anomalies.*
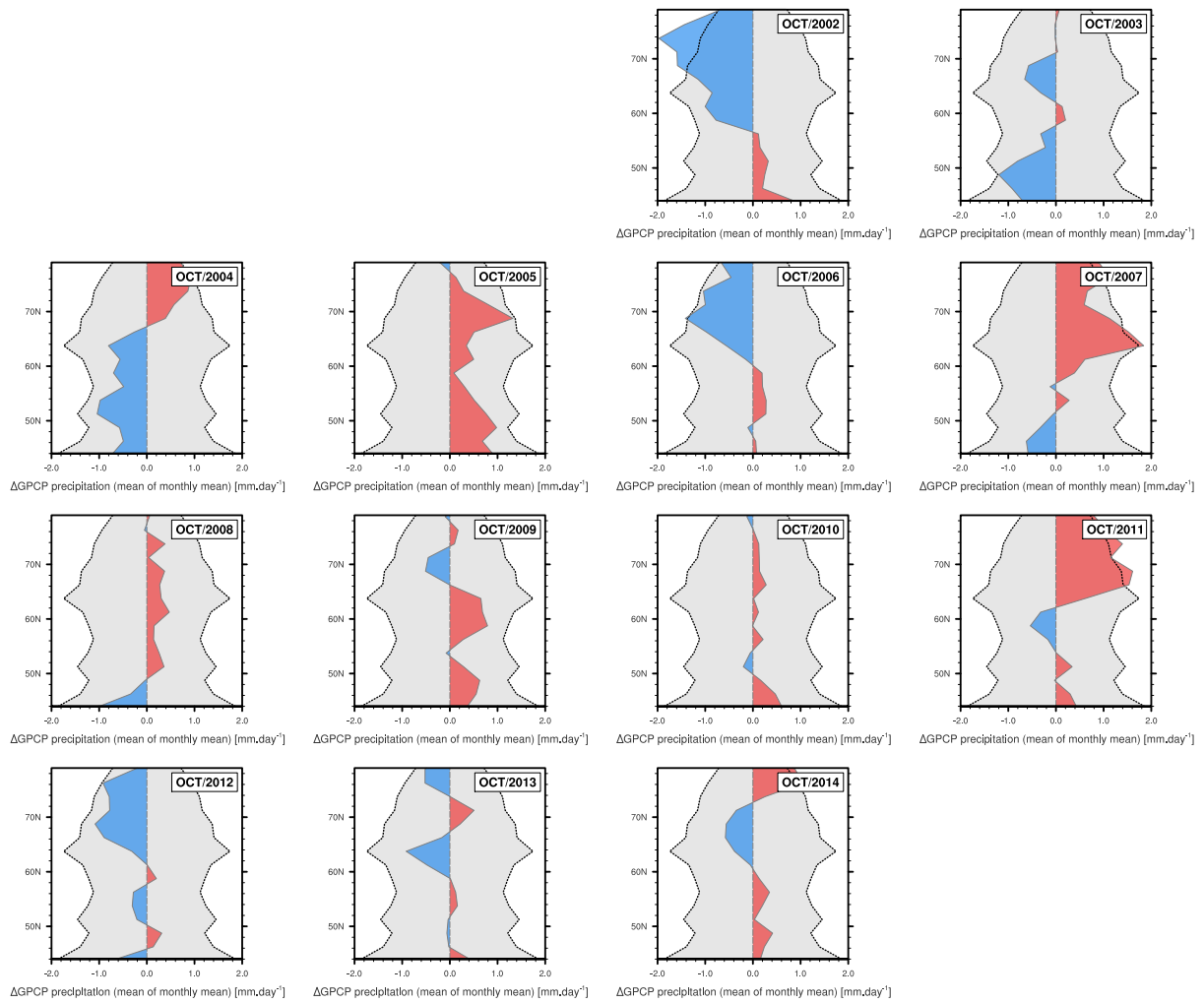
Figures at left show ΔGPCP precipitation (mean of monthly mean) [mm.day⁻¹] for OCT/2002 through OCT/2014.
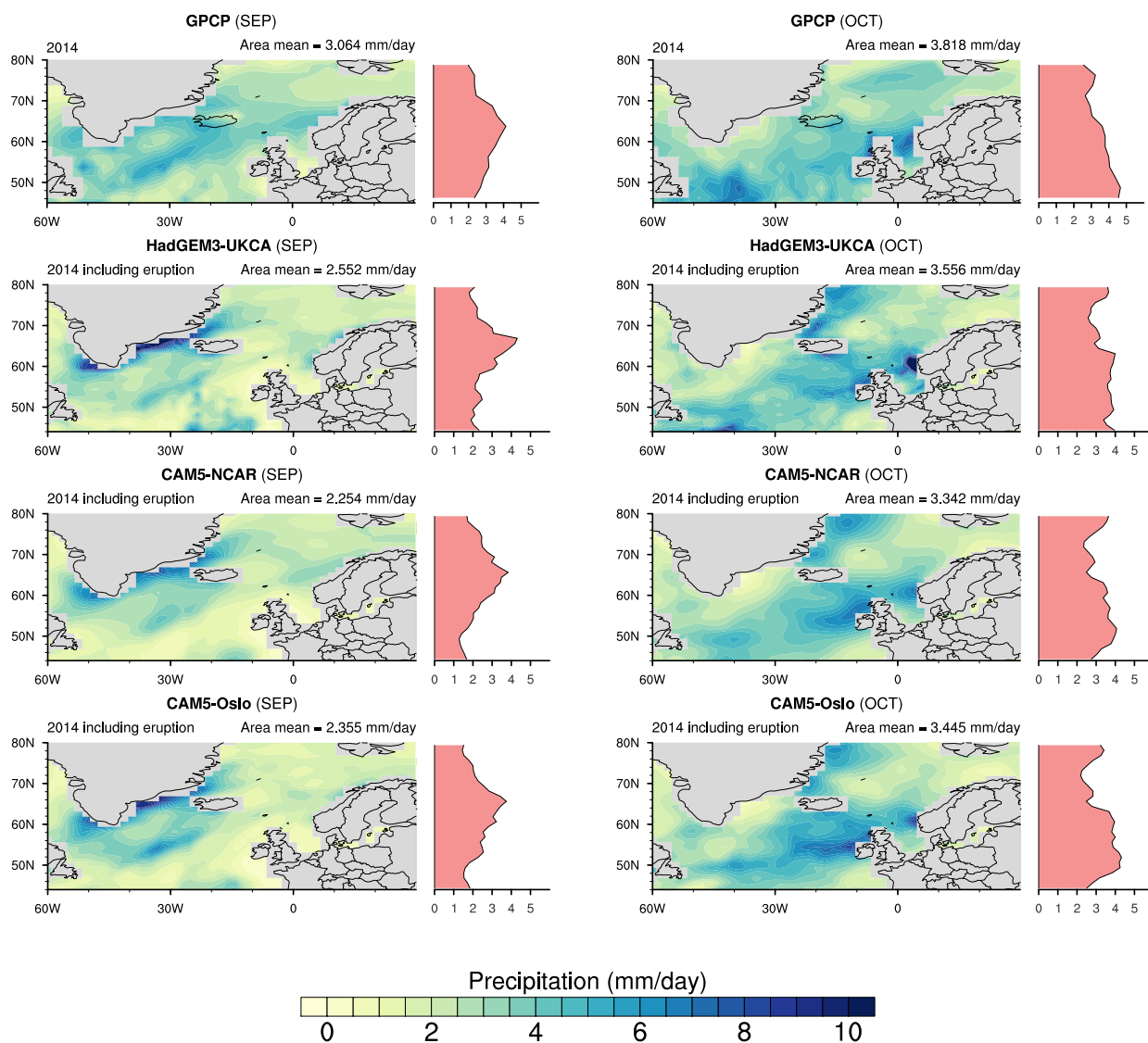
Figure S10.3. continued

Figure S10.4. GPCP and multi-model estimates of the surface precipitation rates. *Monthly mean total precipitation (in mm/day) in 2014 for September (left) and October (right). GPCP (top row), HadGEM3 using UKCA (second row), CAM5-NCAR (third row) and CAM5-Oslo (last row). Modelled precipitation are for the simulations including the eruption.*
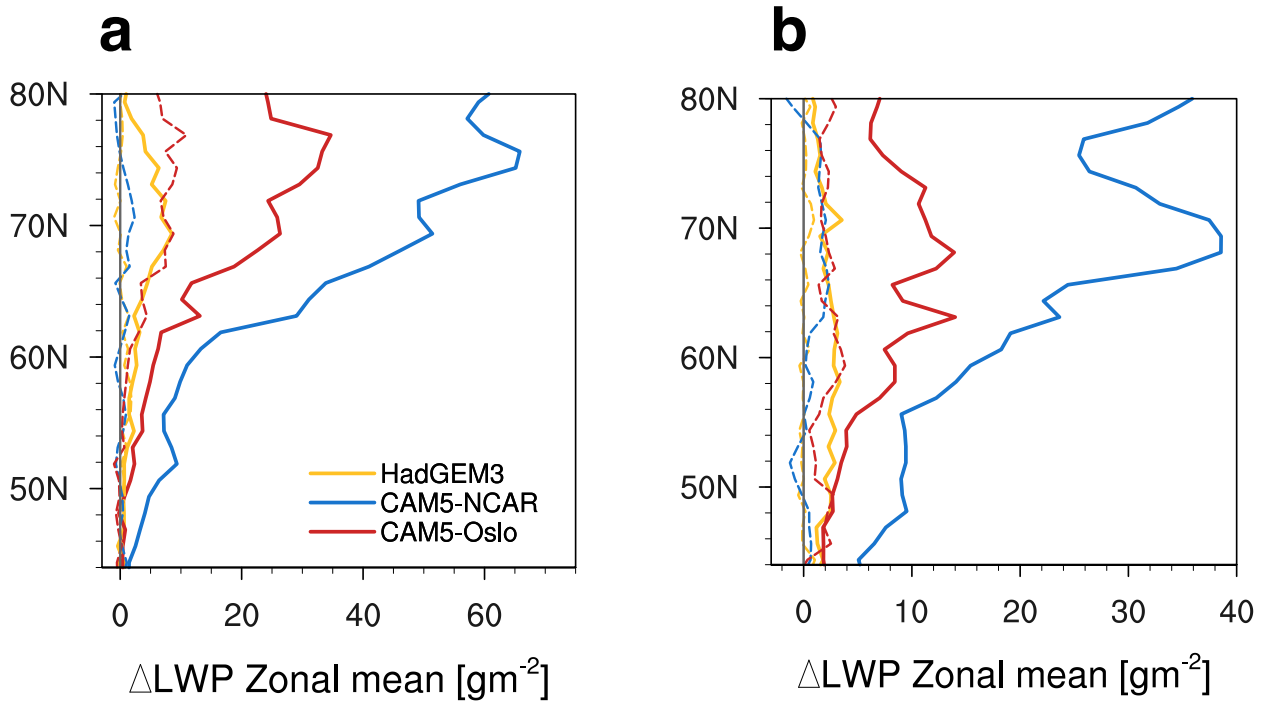
Figure S10.5. Zonal mean of multi-model LWP anomalies considering and excluding the 'lifetime effect'. *Anomalies in g.m⁻² for September (a) and October (b) calculated as the difference between experiment including the eruption minus experiment excluding the eruption for the STAN experiment (plain lines) and the No-Life experiment (dashed lines). Gold lines represent HadGEM3 using UKCA, blue lines represent CAM5-NCAR and red lines represent CAM5-Oslo.*

S11. Factors moderating the radiative forcing from the 2014-15 eruption at Holuhraun

As noted previously[28], the solar insolation falls sharply in October. Thus, if the eruption had commenced in May/June, the radiative forcing would have been greater. In addition, overlying ice clouds reduce any radiative impact of aerosol-cloud interactions in the underlying liquid water clouds as they 'shield' the underlying liquid water clouds from solar insolation. Vertical profiles of the liquid water content and ice water content are shown in Figure S11.1.
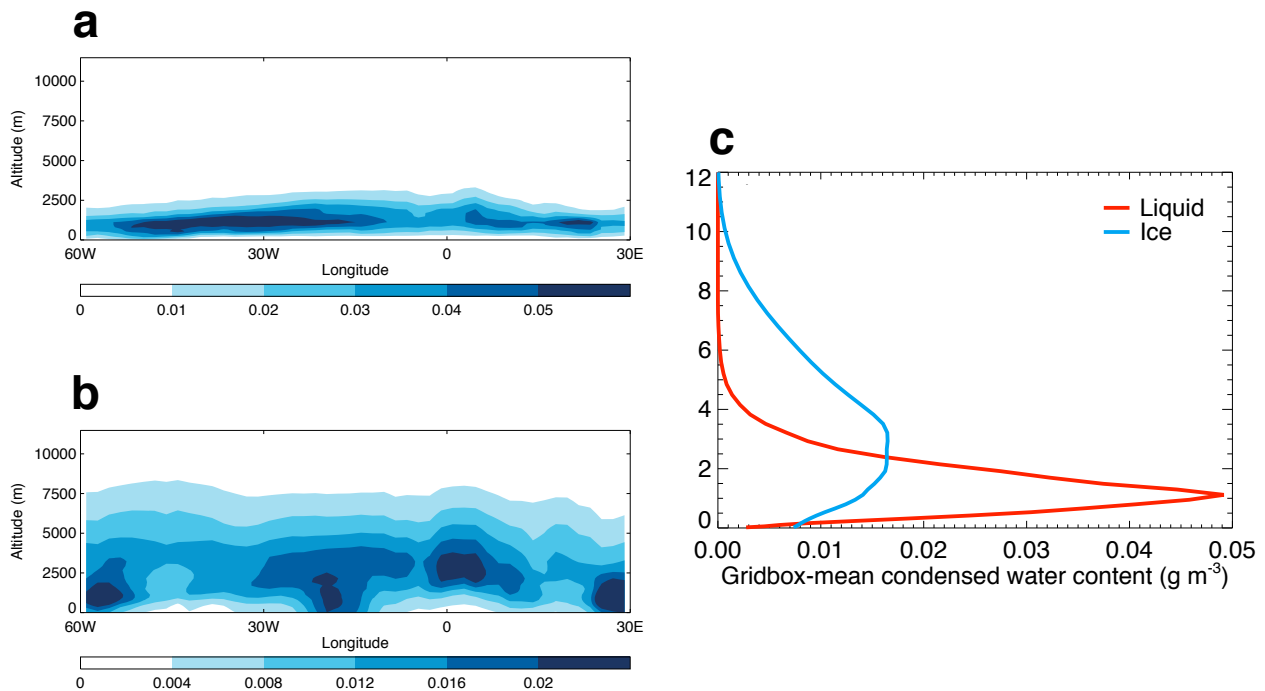

Figure S11.1. The vertical distribution of cloud liquid and ice phases. Showing (a) the meridional cross-section of modelled cloud liquid water content for October 2014, (b) as (a) but for cloud ice water content (note different scale), and c) the mean profile from the area investigated with the red line showing the liquid water and the blue line the ice water.

To investigate the impact of overlying ice clouds, the SOCRATES radiative transfer code[68] was run off-line using a mean water cloud liquid water mass of 3×10^{-4} kg.kg^{-1} in the lowest two kilometres with an overlying ice cloud between 2-4 km with a mean liquid water mass of 1×10^{-4} kg.kg^{-1}, using appropriate solar geometry for Iceland during September, an appropriate vertical profile of water vapour, and an appropriate sea-surface reflectance. Radiative transfer calculations for 'clean' conditions (i.e. excluding emissions from the eruption) used a cloud top r_{eff} of 10.1 μm, and two perturbed cases were assumed to have a Δr_{eff} of -1.4 μm and -3.0 μm (i.e. a r_{eff} of 8.7 μm and 7.1 μm), respectively. These cloud conditions provide a top of atmosphere mean SW upward radiation that is around 85 W.m^{-2}, which is in agreement with CERES observations.

Table S11.1 shows that the impact of overlying ice cloud is to reduce the radiative forcing by a factor of around 0.78 or a 22% reduction, but this factor will of course depend on the fidelity to which the model accurately reproduces cloud ice cloud water path and optical properties, but examining this sensitivity further is beyond the scope of the current paper.

	No eruption r_{eff} = 10.1 µm	Eruption r_{eff} = 8.7 µm (W.m^{-2})	Eruption r_{eff} = 8.7 µm (W.m^{-2})
Including all clouds	84.9	86.7 (-1.8)	89.1 (-4.2)
Excluding Ice clouds	67.5	69.8 (-2.3)	72.8 (-5.3)
Shielding 'factor'		0.78	0.79

Table S11.1. Offline radiative transfer estimates of the effect of overlying clouds. *The top of atmosphere diurnal average outgoing solar flux and the radiative forcing (W.m^{-2}, shown in red), showing the impact of overlying ice clouds.*

S12. Sensitivity of the radiative forcing to the temporal and physical location of the eruption

Here, the sensitivity of the radiative forcing to the temporal and geographic location of the eruption is investigated. Firstly, the eruption is moved backwards by two months to commence at the beginning of June 2014 (Fig. S12b), then it is moved to the coast of Peru (Fig. S12c), and then it is effectively moved back in time so that anthropogenic emissions from 2014 are replaced with those from pre-industrial times (Fig. S12d).
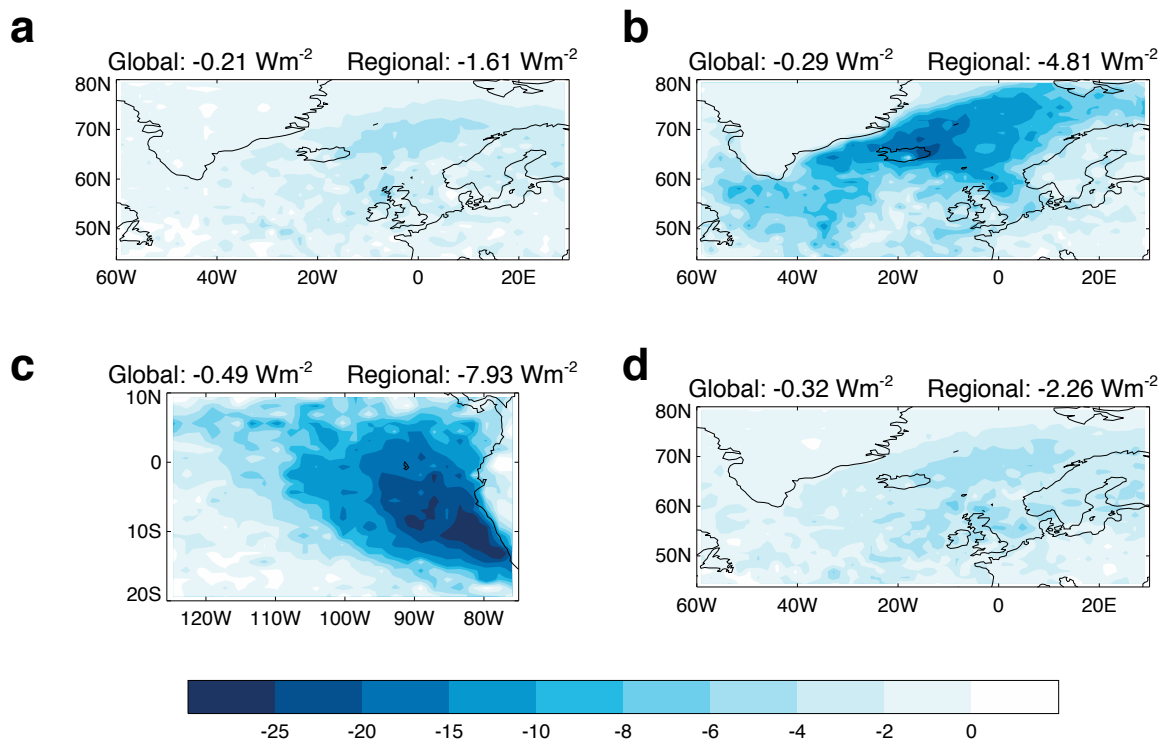

Figure S12.1. Sensitivity of the radiative forcing to the temporal and physical location of the eruption. *The effective radiative forcing (ERF) for September/October 2014 deduced for HadGEM3 for a) STAN simulation, b) using the STAN emission profile, but commencing on 1ˢᵗ June 2014, c) using the STAN emission profile, but eruption located at 15°S, 76°W, d) using the STAN profile, but eruption assumed to be in 1860 (with 2014 meteorology and SSTs assumed). For simulations a-d the change in the LWP is +2.8%, +2.6%, +4.6% and +4.8% respectively.*

S13. Cloud regimes analysis

We go further in answering whether the 2014-15 Holuhraun eruption is a special case by examining the comprehensive analysis of cloud regimes (CRs) prevalent in the region using the analysis method of Oreopoulos and colleagues[44]. This analysis method uses MODIS Collection 006 retrievals of cloud microphysical properties to infer the distinct cloud regimes that are present in any given region. Twelve different prevalent cloud regimes are identified globally consisting of 11 prevalent cloud regimes CR1-CR11, and CR12 which comprises all 2D histograms of small cloud fraction (CF) with no characteristic shape, or the small CF histograms with a dipole pattern where high clouds overlap low clouds.

We present a dedicated CR-based analysis for September and October from multi-year mean data (2002-2014) for AQUA. The CR results from TERRA and AQUA are essentially identical, so only AQUA data are presented here to be consistent with the rest of our analysis.

Figure S13.1 shows, as expected, that the regimes that are dominated by liquid water cloud that could be susceptible to aerosol-cloud-interactions are cloud regimes CR6-CR11, but CR12 also has more liquid than ice in our area of interest.
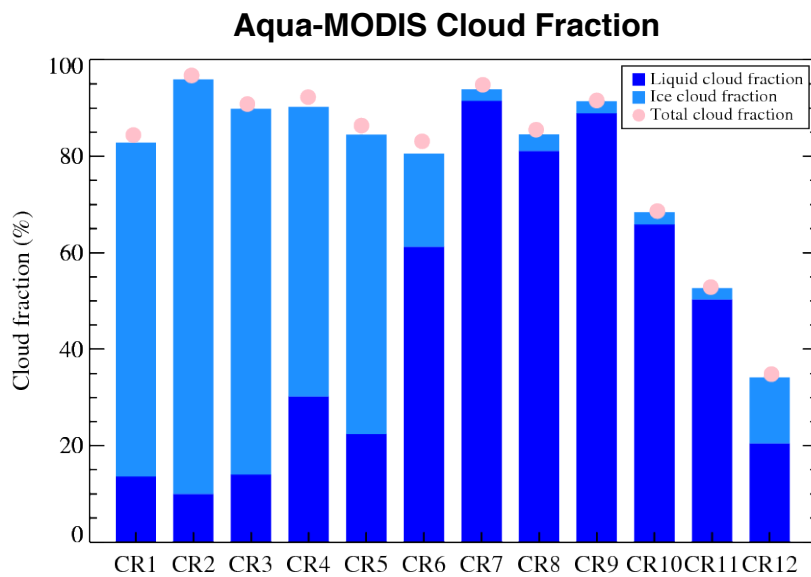

Figure S13.1. The cloud fraction from the different cloud regimes. *The Cloud Regime analysis is derived in the region 44°N-80°N, 60°W-30°E using MODIS AQUA data from 2002-2014 for the September-October months.*

The relative frequency of occurrence (Figure S13.2) shows that CR6, and CR8-11 all exhibit relative frequencies of 5-10%, with CR7 (the least frequent regime globally) showing around 3% relative frequency, and CR12 (when focusing on the yellow dot which represents >80% liquid water cloud, consistent with cloud regimes CR6-CR11) around 15%.

Thus, when examining the 2014-15 Holuhraun eruption, we are far from examining a meteorological 'special case', in fact rather the opposite. We are examining a region that contains the whole spectrum of liquid-dominated cloud regimes and deducing that overall, the impact on LWP is minimal. While Oreopoulos et al., 2017 (in revision) have shown that instantaneous snapshots of cloud properties for these cloud regimes appear distinct under different aerosol loadings, the evolution of the regimes is not tracked temporally as in this study. This study shows that while on one hand the net impact of increased aerosol concentrations on cloud effective radius is significant, the cloud system is well-buffered so that with time it returns to a state where the liquid water path remains essentially unchanged.
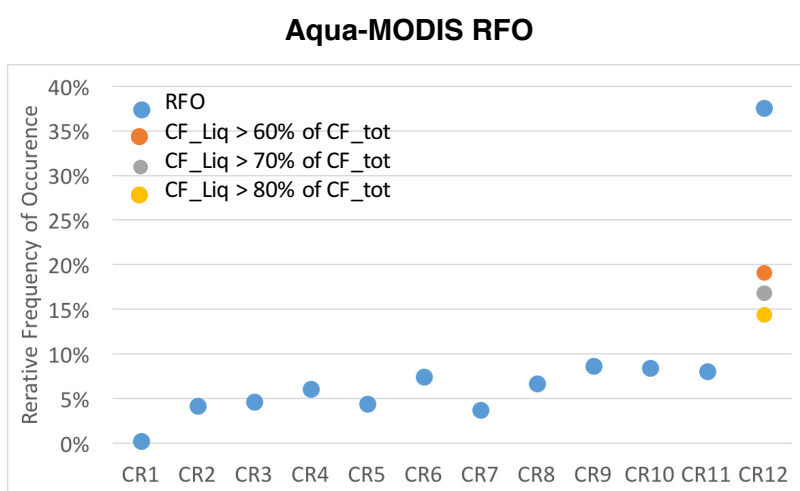

Figure S13.2. The relative frequency of occurrence of the different cloud regimes. *The relative frequency of occurrence (RFO) of the cloud regimes is derived in the region 44°N-80°N, 60°W-30°E using MODIS AQUA data from 2002-2014 for the September-October months.*

S14. The June-August 2008 Kilauea effusive eruption

The eruption of Kilauea and the impact on clouds in the area has been investigated in previous studies[24,45,46]. The effusive eruption of Kilauea during June-August 2008 was notable, but the emissions were around an order of magnitude less than those of the 2014-15 eruption at Holuhraun, being estimated as 10 kt[SO_2]/day over a period of around 3 months[24]. Thus, one might not expect any significant climate impact from Kilauea, but one might expect a perturbation to r_{eff} (first indirect effect) and LWP (if second indirect effects play a part). We have repeated our analysis (see Supplementary S4) using the MODIS AQUA data (Supplementary M4) for the Kilauea eruption. Changes in cloud properties are calculated for the June-August (JJA) period for the years covering the period from 2003 to 2015. Difference in cloud properties (Δr_{eff} and ΔLWP) for each individual JJA season are derived as the difference in annual JJA mean from the multi-year (2003-2015) JJA mean (excluding 2008). Figure S14.1 shows that r_{eff} in 2008 is perturbed as per previous analyses[24,45], but the LWP (Figure S14.2) is only marginally influenced with a zonal mean perturbation over the three months of less than 5 g.m^{-2}. The main conclusion that can be drawn from this is that again, the LWP is close to invariant despite the increase in aerosol concentration associated with the significantly elevated levels of SO_2 emission.

The results of the cloud regime analysis (Supplementary S13) are also shown for Kilauea for the June-July-August period from multi-year mean data (2003-2014) relevant to our investigation (Figure S14.3). Here rather than all cloud regimes being present, the liquid cloud regime is dominated by CR10, CR11 and CR12. So, while this case (examined by Yuan and colleagues[24]) might be considered a special case, the 2014-15 Holuhraun case is wholly more general.
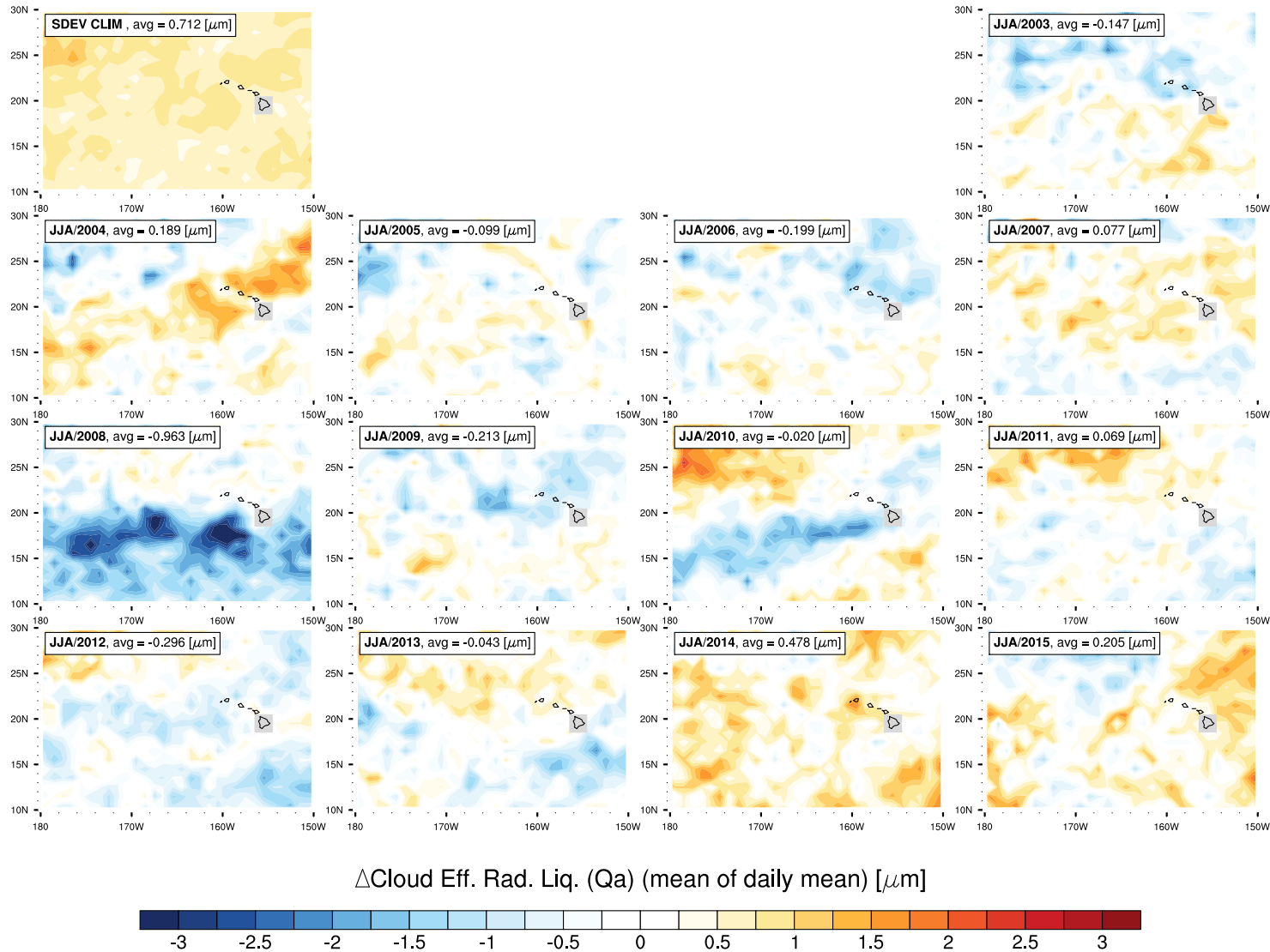
Figure S14.1. The effective radius anomalies during the June-August (JJA) season from MODIS. *Showing Δr_eff (in μm) and associated zonal mean (continued). Anomalies for each individual JJA season are derived as the difference in annual JJA mean from the 2003-2015 (excluding 2008) JJA mean. The grey shading in the zonal mean represent the standard deviation over the 2003-2015 period.*

JJA/2003

△Cloud Eff. Rad. Liq. (Qa) (mean of daily mean) [μm]

JJA/2004

△Cloud Eff. Rad. Liq. (Qa) (mean of daily mean) [μm]

JJA/2005

△Cloud Eff. Rad. Liq. (Qa) (mean of daily mean) [μm]

JJA/2006

△Cloud Eff. Rad. Liq. (Qa) (mean of daily mean) [μm]

JJA/2007

△Cloud Eff. Rad. Liq. (Qa) (mean of daily mean) [μm]

JJA/2008

△Cloud Eff. Rad. Liq. (Qa) (mean of daily mean) [μm]

JJA/2009

△Cloud Eff. Rad. Liq. (Qa) (mean of daily mean) [μm]

JJA/2010

△Cloud Eff. Rad. Liq. (Qa) (mean of daily mean) [μm]

JJA/2011

△Cloud Eff. Rad. Liq. (Qa) (mean of daily mean) [μm]

JJA/2012

△Cloud Eff. Rad. Liq. (Qa) (mean of daily mean) [μm]

JJA/2013

△Cloud Eff. Rad. Liq. (Qa) (mean of daily mean) [μm]

JJA/2014

△Cloud Eff. Rad. Liq. (Qa) (mean of daily mean) [μm]

JJA/2015

△Cloud Eff. Rad. Liq. (Qa) (mean of daily mean) [μm]

Figure S14.1. *continued*

Figure S14.2. The liquid water path anomalies during the June-August (JJA) season from MODIS. *Showing ΔN$_d$ (in cm^{-3}) and associated zonal mean (continued). Anomalies for each individual JJA season are derived as the difference in annual JJA mean from the 2003-2015 (excluding 2008) JJA mean. The grey shading in the zonal mean represent the standard deviation over the 2003-2015 period.*
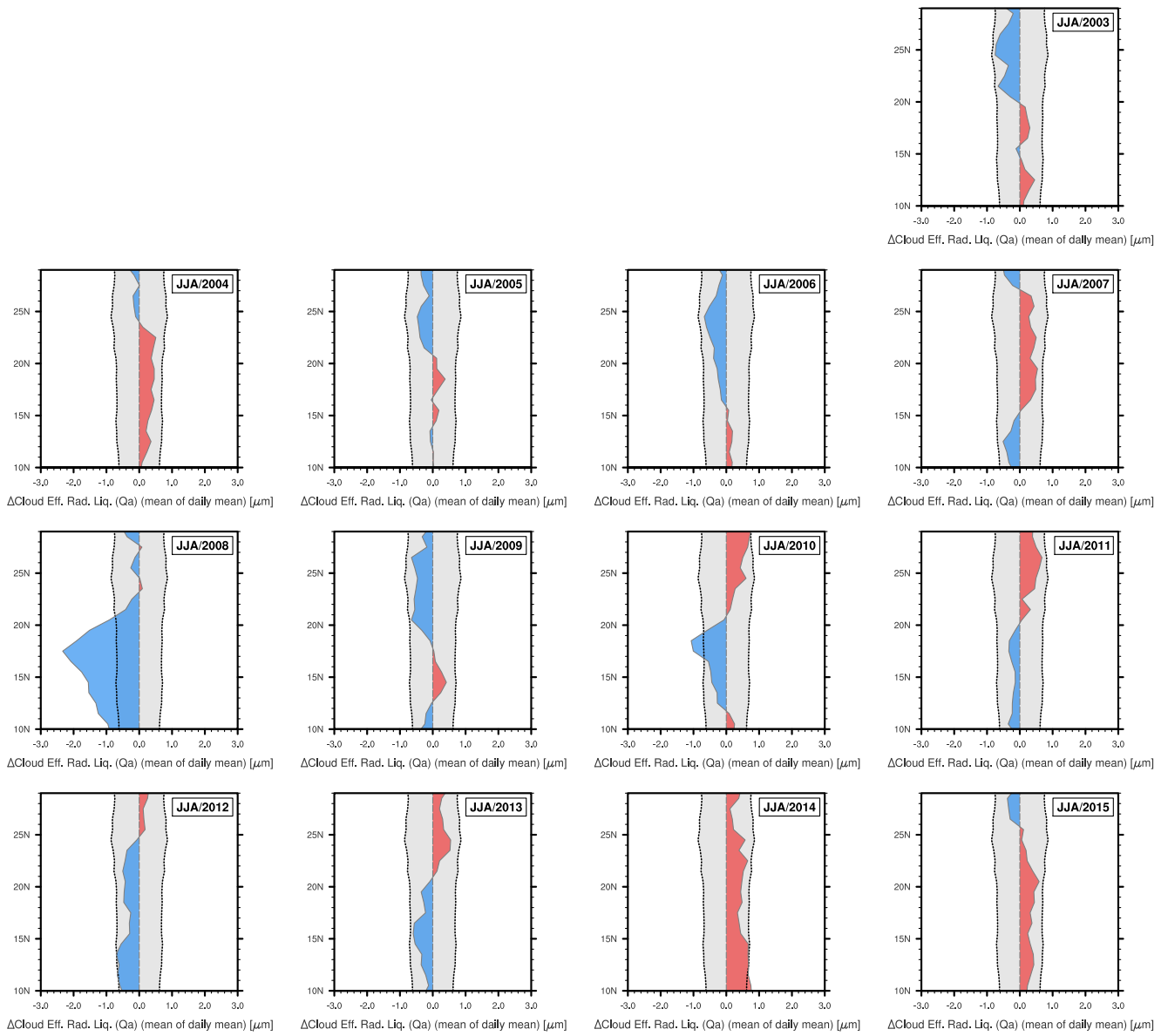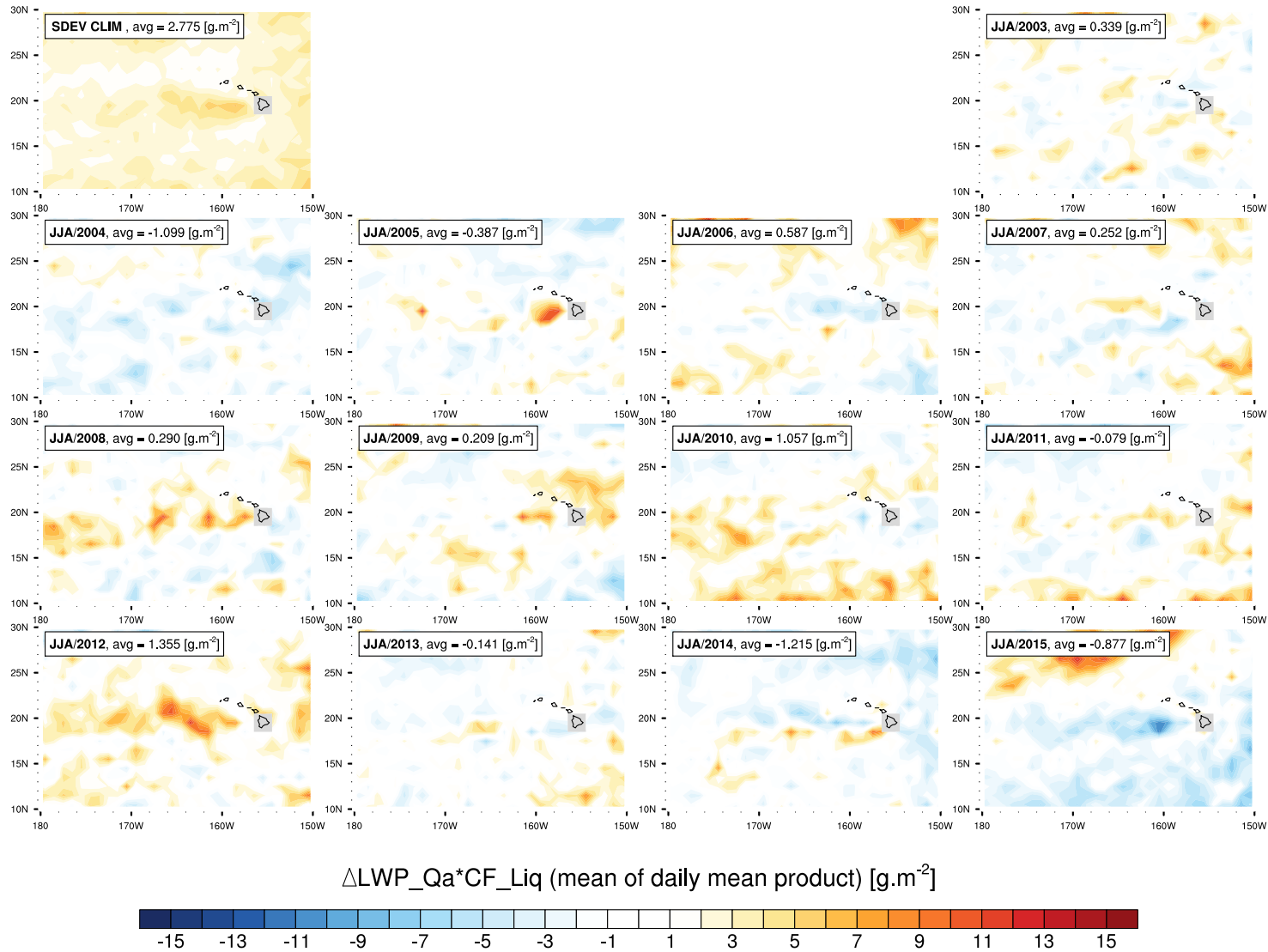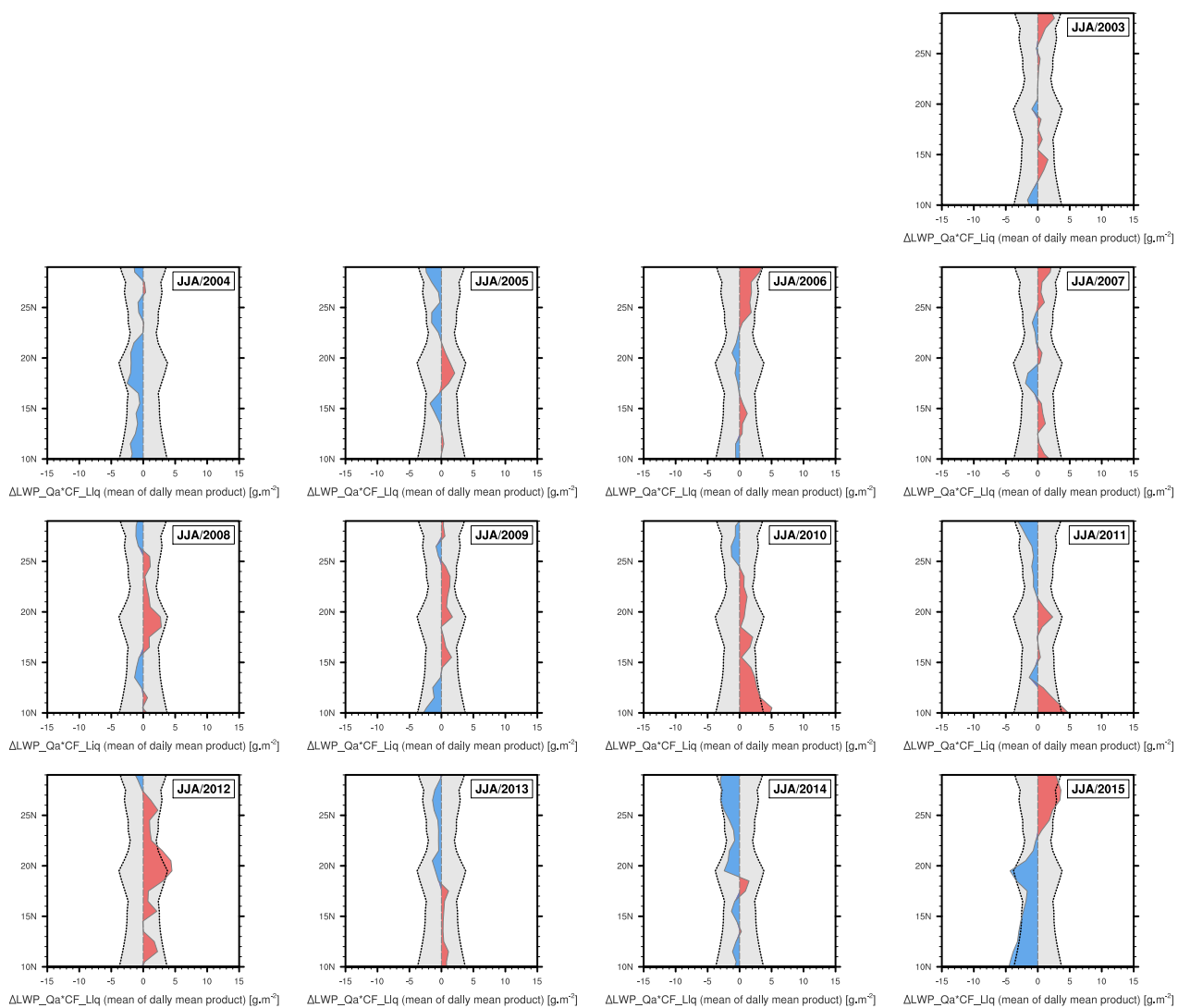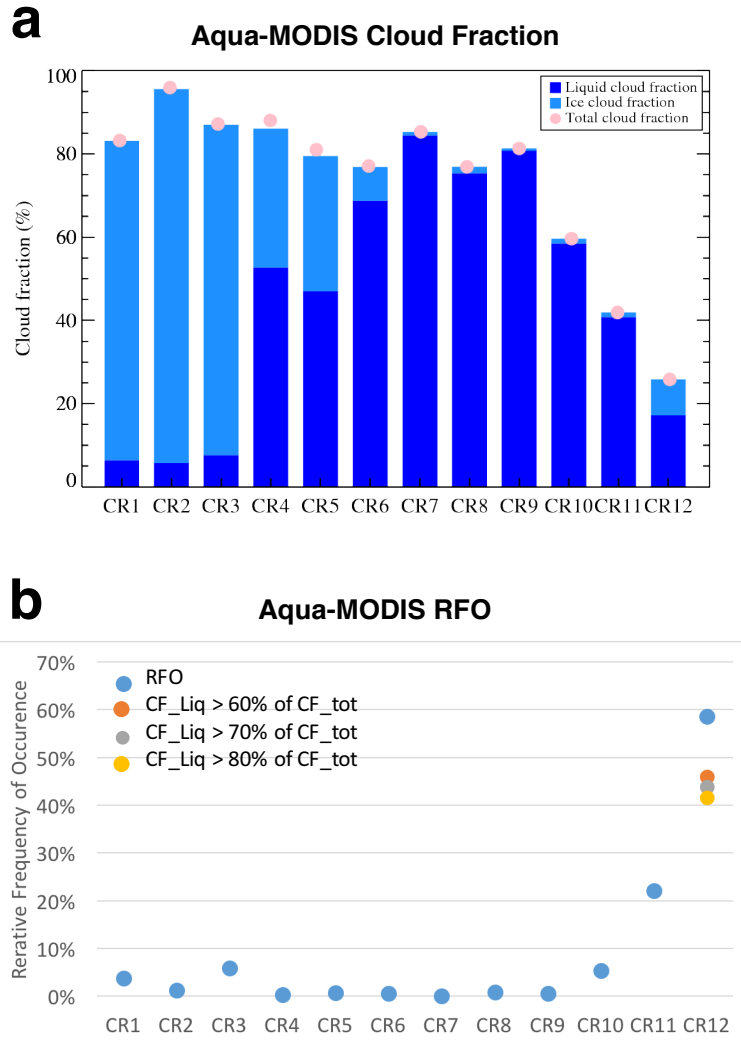
Figure S14.2. *continued*

Figure S14.3. The cloud regimes analysis applied to the surrounding of Kilauea. *Showing the cloud fraction from the different cloud regimes (a) and the relative frequency of occurrence of the different cloud regimes derived in the region 10°N-30°N, 180°W-150°W using MODIS AQUA data from 2003-2015 for the JJA seasons.*

Section S15. Developing estimates of uncertainty

While our HadGEM3 STAN simulations provide results that are in reasonable agreement with the observations, there are parametric uncertainties associated with assumptions about the emission rates of SO_2 and the plume top height. These uncertainties are due to the incomplete nature of observations during the eruption. Figure S15.1 shows graphical representations of the uncertainties associated with each.
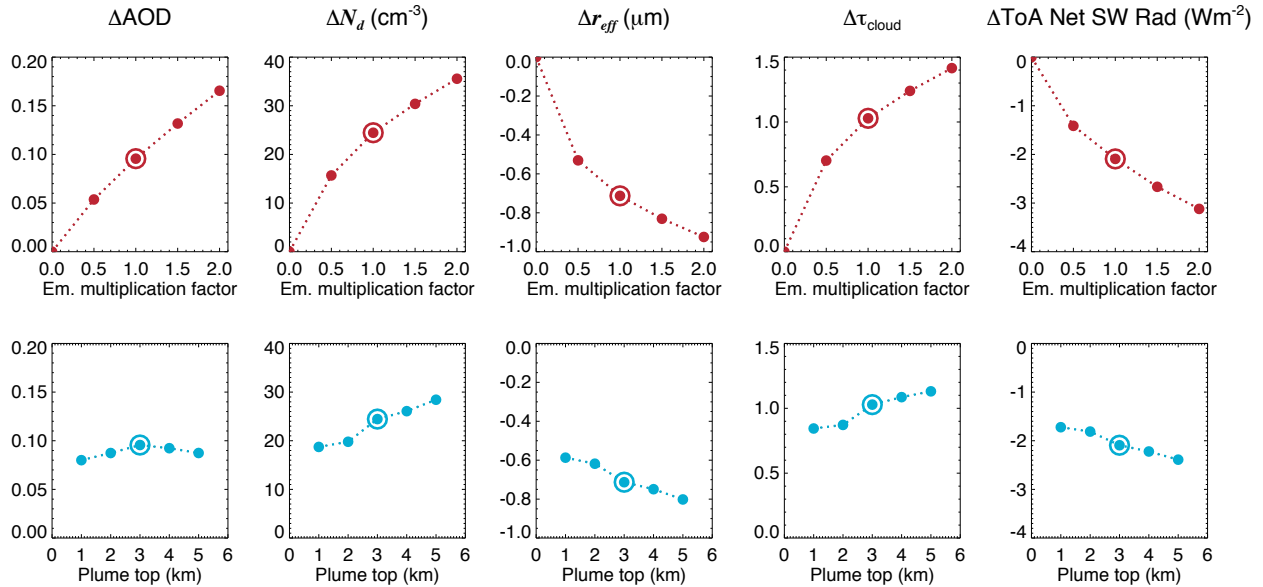

***Figure S15.1. HadGEM3 sensitivity to volcanic SO_2 emission rates and injection height.** Showing the sensitivity of ΔAOD, ΔN_d, Δr_{eff}, $\Delta \tau_{cloud}$, and ΔToA_{SW} for top row) changes in SO_2 emission rates (characterised by the emission multiplication factor) and bottom row) changes in the assumed emission top height. The values used in STAN are circled.*

STAN and 95% Uncertainty	ΔAOD	ΔN_d	Δr_{eff}	$\Delta \tau_{cloud}$	ΔToA_{SW} local	ΔToA_{SW} global
Emissions of SO_2	TH15 ± 50%	41%	30%	20%	26%	26%	50%
Plume top (km)	3km ± 1km	6%	12%	9%	10%	6%	23%
Total uncertainty		x1.5	x1.4	x1.3	x1.4	x1.3	x1.8

***Table S15.1. Impacts of input parameter uncertainty in the HadGEM3 model using UKCA.** Showing the impact on ΔAOD, ΔN_d, Δr_{eff}, $\Delta \tau_{cloud}$, and ΔToA_{SW}. The total uncertainty is quoted as a factor (e.g. x1.3 for Δr_{eff}).*

Table S15.1 shows the percentage uncertainty derived assuming that the emissions are uncertain (at 95% confidence) to 50% and the plume top ranges is 3 ± 1 km.

Our modelling study suggests that for the period of investigation the mean Δr_{eff} over ocean areas for the region of investigation can be quoted as -0.67 ± 0.2 μm when meteorological variability is not included or -0.96 ± 0.3 μm when meteorological variability is included, which in agreement with MODIS values of -0.98 μm. The estimates of the effective radiative forcing (ERF) may also be computed directly from the model. Over the domain of investigation, we estimate an ERF of -2.1 ± 0.6 W.m^{-2} while over the global domain we estimate -0.21 ± 0.16 W.m^{-2} or a 2014 global annual average of -0.04 ± 0.03 W.m^{-2}.

The 2014-15 eruption at Holuhraun yields a global annual mean radiative forcing efficiency of -0.0088 ± 0.0024 W.m^{-2}/TgSO$_2$ (see main text). The similarity with the IPCC estimate[17,47] (i.e. -0.009 W.m^{-2}/TgSO$_2$) is remarkable, but may be by chance given the modelled sensitivity to emission location and time (Supplementary S12). Note that the ERF from all anthropogenic aerosols is rather similar to the ERF from only sulphate aerosols as it has been shown in the fifth IPCC assessment report[17] (see Table 7.5 therein).

Code availability

HadGEM3 and SOCRATES code are available from https://code.metoffice.gov.uk/ for registered users. To register for an account, users should contact their local institutional sponsor. If in doubt, please contact Scientific_Partnerships@metoffice.gov.uk for advice stating your affiliate institution and your reason for wanting access. CAM-NCAR is the atmospheric component of CESM1.0 which code is available at: http://www.cesm.ucar.edu/models/cesm1.0/. The NorESM code is available for registered users through signing a respective license. In order to initiate this process please contact noresm-ncc@met.no. Users should briefly state the purpose of the use of the model. All NorESM users need also to register themselves as a CESM user at the CESM website (http://www.cesm.ucar.edu/models/register/register.html). Persons who use the marine biogeochemstry component HAMOCC in NorESM on addition need to sign the MPI-ESM license (at https://www.mpimet.mpg.de/en/science/models/mpi-esm/).

Data availability

The MODIS cloud and aerosol products (dx.doi.org/10.5067/MODIS/MYD06_L2.006) are the 1 degree Level 3.0 collection version 051 datasets available from ftp://ladsweb.nascom.nasa.gov/allData/51/MYD08_M3/. The CERES radiation data are the SSF 1 degree Terra Edition 2.8 available from https://ceres.larc.nasa.gov/order_data.php. GPCP version 2.3 combined precipitation data set are available from https://www.esrl.noaa.gov/psd/data/gridded/data.gpcp.html. The IASI retrievals of SO_2 column loading are available from the corresponding author upon reasonable request.

Supplementary references

[50]Bauduin, S. *et al.*, Retrieval of near-surface sulfur dioxide (SO2) concentrations at a global scale using IASI satellite observations. *Atmos. Meas. Tech.*, 9, 721-740, doi:10.5194/amt-9-721-2016 (2016).

[51]Clarisse, L., Coheur, P.-F., Theys, N., Hurtmans, D., and Clerbaux, C., The 2011 Nabro eruption, a SO2 plume height analysis using IASI measurements. *Atmos. Chem. Phys.*, 14, 3095-3111, doi:10.5194/acp-14-3095-2014 (2014).

[52]Bauduin, S.; Clarisse, L.; Clerbaux, C.; Hurtmans, D. and Coheur, P.-F, IASI observations of sulfur dioxide (SO2) in the boundary layer of Norilsk. *J. Geophys. Res.*, 119, 4253-4263 (2014).

[53]Anderson, G., Clough, S., Kneizys, F., Chetwynd, J. and Shettle, E.P., AFGL Atmospheric Constituent Profiles (0-120km), AFGL-TR-86-0110. Environmental Research Papers, 954, ADA175173 (1986).

[54]Collins, W. J. *et al.*, Development and evaluation of an Earthsystem model-HadGEM2. *Geophys. Model Dev.*, 4, 997–1062 (2011).

[55]Khairoutdinov, M., and Y. Kogan, A new cloud physics parameterization in a large-eddy simulation model of marine stratocumulus. *Mon. Wea. Rev.*, 128, 229-243, doi: http://dx.doi.org/10.1175/1520-0493 (2000).

[56]Williams, K. D. *et al.*, The Met Office Global Coupled model 2.0 (GC2) configuration. *Geosci. Model. Dev.*, 8, 1509-1524, doi:10.5194/gmd-8-1509-2015 (2015).

[57]Zerroukat, M. and T. Allen, On the monotonic and conservative transport on overset Yin-Yang grids. *Journal of Computational Physics*, 302, 285-299, doi:10.1016/j.jcp.2015.09.006 (2015).

[58]Jones, C. D. *et al.*, The HadGEM2-ES implementation of CMIP5 centennial simulations. *Geoscientific Model Development,* 4, no. 3: 543-570, doi:10.5194/gmd-4-543-2011 (2011).

[59]Telford, P., P. Braesicke, O. Morgenstern, and J. Pyle, Technical note: Description and assessment of a nudged version of the new dynamics Unified Model. *Atmos. Chem. Phys.*, 8, 1,701–1,712 (2008).

[60]Dee, D. P. *et al.*, The ERA-Interim reanalysis: configuration and performance of the data assimilation system. *Q. J. R. Meteorol. Soc.*, 137, 553-597, doi: 10.1002/qj.828 (2011).

[61]Rayner, N. A. *et al.*, Global analyses of sea surface temperature, sea ice, and night marine air temperature since the late nineteenth century. *J. Geophys. Res.*, 108, 4407, D14, doi: 10.1029/2002JD002670 (2003).

[62]Gilleland, E., D. Ahijevych, B.G. Brown, B. Casati, and E.E. Ebert, Intercomparison of spatial forecast verification methods. *Wea. Forecasting*, 24, 1416–1430. doi: http://dx.doi.org/10.1175/2009WAF2222269.1 (2009).

[63]Boers, R., Acarreta, J. R., and Gras, J. L., Satellite monitoring of the first indirect aerosol effect: retrieval of the droplet concentration of water clouds. *J. Geophys. Res.-Atmos.*, 111, D22208, doi: 10.1029/2005jd006838, 2006. 306, 307, 339 (2006).

[64]Grosvenor, D. P., & Wood, R., The effect of solar zenith angle on MODIS cloud optical and microphysical retrievals within marine liquid water clouds. *Atmospheric Chemistry and Physics*, 14(14), 7291-7321 (2014).

[65]Jones, A., Roberts, D. L., Woodage, M. J., and Johnson, C. E., Indirect sulphate aerosol forcing in a climate model with an interactive sulphur cycle. J. Geophys. Res: Atm., 106(D17), 20293-20310 (2001).

[66]Morrison, H., and Gettelman, A., A new two-moment bulk stratiform cloud microphysics scheme in the Community Atmosphere Model, Version 3 (CAM3). Part I: Description and numerical tests. J. Clim. 21, 3642–3659 (2008).

[67]Boutle, I. A., Abel, S. J., Hill, P. G., and Morcrette, C. J., Spatial variability of liquid cloud and rain: observations and microphysical effects. Q. J. R. Meteorol. Soc., 140, 583–594, DOI:10.1002/qj.2140 (2014).

[68]Edwards, J. M. and Slingo, A., Studies with a flexible new radiation code. I: Choosing a configuration for a large-scale model. Q. J. Roy. Meteorol. Soc., 122:689–719 (1996).